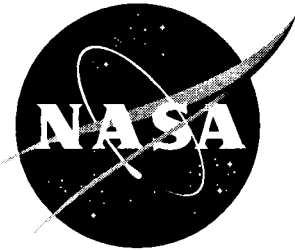


NASA/TM-2003-212431



Summary of EASM Turbulence Models in CFL3D With Validation Test Cases

*Christopher L. Rumsey and Thomas B. Gatski
Langley Research Center, Hampton, Virginia*

June 2003

The NASA STI Program Office . . . in Profile

Since its founding, NASA has been dedicated to the advancement of aeronautics and space science. The NASA Scientific and Technical Information (STI) Program Office plays a key part in helping NASA maintain this important role.

The NASA STI Program Office is operated by Langley Research Center, the lead center for NASA's scientific and technical information. The NASA STI Program Office provides access to the NASA STI Database, the largest collection of aeronautical and space science STI in the world. The Program Office is also NASA's institutional mechanism for disseminating the results of its research and development activities. These results are published by NASA in the NASA STI Report Series, which includes the following report types:

- **TECHNICAL PUBLICATION.** Reports of completed research or a major significant phase of research that present the results of NASA programs and include extensive data or theoretical analysis. Includes compilations of significant scientific and technical data and information deemed to be of continuing reference value. NASA counterpart of peer-reviewed formal professional papers, but having less stringent limitations on manuscript length and extent of graphic presentations.
- **TECHNICAL MEMORANDUM.** Scientific and technical findings that are preliminary or of specialized interest, e.g., quick release reports, working papers, and bibliographies that contain minimal annotation. Does not contain extensive analysis.
- **CONTRACTOR REPORT.** Scientific and technical findings by NASA-sponsored contractors and grantees.

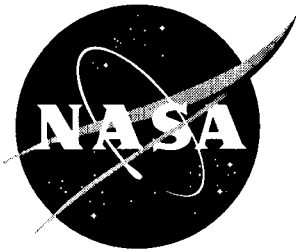
- **CONFERENCE PUBLICATION.** Collected papers from scientific and technical conferences, symposia, seminars, or other meetings sponsored or co-sponsored by NASA.
- **SPECIAL PUBLICATION.** Scientific, technical, or historical information from NASA programs, projects, and missions, often concerned with subjects having substantial public interest.
- **TECHNICAL TRANSLATION.** English-language translations of foreign scientific and technical material pertinent to NASA's mission.

Specialized services that complement the STI Program Office's diverse offerings include creating custom thesauri, building customized databases, organizing and publishing research results ... even providing videos.

For more information about the NASA STI Program Office, see the following:

- Access the NASA STI Program Home Page at <http://www.sti.nasa.gov>
- E-mail your question via the Internet to help@sti.nasa.gov
- Fax your question to the NASA STI Help Desk at (301) 621-0134
- Phone the NASA STI Help Desk at (301) 621-0390
- Write to:
NASA STI Help Desk
NASA Center for AeroSpace Information
7121 Standard Drive
Hanover, MD 21076-1320

NASA/TM-2003-212431



Summary of EASM Turbulence Models in CFL3D With Validation Test Cases

*Christopher L. Rumsey and Thomas B. Gatski
Langley Research Center, Hampton, Virginia*

National Aeronautics and
Space Administration

Langley Research Center
Hampton, Virginia 23681-2199

June 2003

Contents

ABSTRACT	iv
1 INTRODUCTION	1
2 OVERVIEW OF CFL3D	2
3 THE EASM EXPLICIT ALGEBRAIC STRESS MODELS	4
4 VALIDATION TEST CASES	7
4.1 Flat Plate	7
4.2 Back Step	10
4.3 Transonic Diffuser	13
4.4 NACA 4412 Airfoil	19
4.5 Ejector Nozzle	21
4.6 Axisymmetric Bump	22
4.7 ONERA M6 Wing	27
4.8 2-D Airfoil Wake	30
4.9 Curved Duct in Zero Pressure Gradient	31
5 CONCLUSIONS	36

ABSTRACT

This paper summarizes the Explicit Algebraic Stress Model in $K-\omega$ form (EASM-ko) and in $K-\varepsilon$ form (EASM-ke) in the Reynolds-averaged Navier-Stokes code CFL3D. These models have been actively used over the last several years in CFL3D, and have undergone some minor modifications during that time. Details of the equations and method for coding the latest versions of the models are given, and numerous validation cases are presented. This paper serves as a validation archive for these models.

1 INTRODUCTION

A turbulence model must be employed in conjunction with the Reynolds-averaged Navier-Stokes (RANS) equations in order to close the equations. Over the last 30 years, many different turbulence models have been developed for use with RANS. Because there are so many to choose from, it is sometimes difficult for a CFD user to decide which model to use for a given flow situation.

It is therefore very important that new (as well as existing) models be thoroughly validated in all the CFD codes into which they are implemented. This validation process should consist of applications to a suite of as many test cases as possible, which, taken together, thoroughly exercise the capabilities of the turbulence model.

Most turbulence models for use with RANS today are linear eddy viscosity models, which assume a Boussinesq relationship between the turbulent stresses and mean strain rate tensor through the use of an isotropic eddy viscosity. Recently, however, nonlinear eddy viscosity models have been gaining widespread attention. This class of models assumes a higher-order tensor representation involving either powers of the mean velocity gradient or combinations of the mean strain rate and rotation rate tensors.

One of the advantages of nonlinear eddy viscosity models over linear eddy viscosity models is that nonlinear models can predict differences in the turbulent normal stresses. Although this deficiency in linear models is not generally considered important for most external aerodynamic problems of interest, it has been shown to be crucial for capturing secondary motion in a corner flow, which is driven by the gradient of the turbulent normal stresses (see Abdol-Hamid et al.[1]).

Explicit algebraic stress models (EASM) belong to the class of nonlinear eddy viscosity models. However, unlike some nonlinear models which determine their expansion coefficients through calibration with experimental or numerical data, EASMs obtain their expansion coefficients through their rigorous relationship with their “parent” full differential Reynolds stress equations. See Gatski and Rumsey [2] for details.

The EASM models, when originally conceived [3], were solved by assuming a fixed (equilibrium) value of \mathcal{P}/ε when determining the parameter $g = (C_1/2 + \mathcal{P}/\varepsilon - 1)^{-1}$. This “fixed- g ” EASM model was subsequently improved [4, 5, 6] by allowing \mathcal{P}/ε to vary. It is only this latter method, sometimes referred to as “variable- g ” EASM, that is discussed in this report. The “fixed- g ” EASM method has also been coded into CFL3D, but it is generally no longer recommended and will not be discussed. Other applications of EASM (using variable- g) can be found in Carlson [7] and Carlson et al.[8].

The purpose of this paper is primarily as a validation archive for the EASM-ko and EASM-ke models as coded in CFL3D. Thus, engineers who attempt to code these turbulence models for themselves in their own CFD codes can use this paper as a reference for the results they should expect to get with these models. This paper is not intended to advocate EASM, or to point out cases for which EASM yields improved (or worse) results than more conventional models. Therefore, no comparisons are presented between EASM and other models. That exercise is left to the reader. Here, the two versions of EASM-ko and EASM-ke are compared only with each other (and with experiment or theory).

The next two sections describe the formulas for the EASM-ko and EASM-ke models, including details regarding the numerical method employed to solve them in CFL3D. Following that,

the models are applied to several test cases. Then, conclusions are drawn in the last section.

2 OVERVIEW OF CFL3D

The computer code CFL3D [9] solves the three-dimensional, time-dependent, Reynolds averaged compressible Navier-Stokes equations with an upwind finite-volume formulation (it can also be exercised in two-dimensional mode of operation for 2-D cases). It can solve flows over multiple-zone grids that are connected in a one-to-one, patched, or overset manner, and can employ grid sequencing, multigrid, and local time stepping when accelerating convergence to steady state. Upwind-biased spatial differencing is used for the inviscid terms, and flux limiting is used to obtain smooth solutions in the vicinity of shock waves, when present. Viscous terms are centrally differenced, and cross-diffusion terms are neglected. For very low Mach number flows, preconditioning [10] is used to insure convergence and accuracy of the solutions.

The CFL3D code is advanced in time with an implicit approximate factorization method. The implicit derivatives are written as spatially first-order accurate, which results in block tridiagonal inversions for each sweep. However, for solutions that utilize Roe flux-difference splitting [11], the block tridiagonal inversions are further simplified using a diagonal algorithm with a spectral radius scaling of the viscous terms. All solutions in this paper use Roe.

Following Wilcox [12], Reynolds averaging can be used with the Navier-Stokes equations in Favre variables [13] to account for turbulent fluctuations. The resulting equations of motion can be written using the summation convention as follows. The full Navier-Stokes equations are shown here, but in CFL3D they are solved using the thin-layer approximation in pre-selected coordinate direction(s). The equations are given here in terms of dimensional quantities. Although not shown, the equations are subsequently nondimensionalized and solved in generalized coordinates (see Krist et al.[9]).

$$\frac{\partial \rho}{\partial t} = \frac{\partial}{\partial x_j}(\rho u_j) = 0 \quad (1)$$

$$\frac{\partial}{\partial t}(\rho u_i) + \frac{\partial}{\partial x_j}(\rho u_j u_i) = -\frac{\partial p}{\partial x_i} - \frac{\partial \tau_{ij}}{\partial x_j} \quad (2)$$

$$\frac{\partial}{\partial t}(\rho E) + \frac{\partial}{\partial x_j}(\rho u_j H) = \frac{\partial}{\partial x_j}(-u_i \tau_{ij} - \dot{q}_j + \psi_j), \quad (3)$$

where

$$p = (\gamma - 1) \left[\rho E - \frac{1}{2} \rho (u^2 + v^2 + w^2) - \rho K \right] \quad (4)$$

$$E = e + \frac{1}{2} (u^2 + v^2 + w^2) + K \quad (5)$$

$$H = E + p/\rho \quad (6)$$

$$\dot{q}_j = -\frac{1}{\gamma - 1} \left(\frac{\mu}{Pr} + \frac{\mu_t^*}{Pr_t} \right) \frac{\partial a^2}{\partial x_j} \quad (7)$$

$$a^2 = \frac{\gamma p}{\rho} \quad (8)$$

$$\psi_j = \left(\mu + \frac{\mu_t^*}{\sigma_K} \right) \frac{\partial K}{\partial x_j}, \quad (9)$$

where σ_K is defined in the next section. Define:

$$S_{ij} = \frac{1}{2} \left(\frac{\partial u_i}{\partial x_j} + \frac{\partial u_j}{\partial x_i} \right) \quad (10)$$

$$W_{ij} = \frac{1}{2} \left(\frac{\partial u_i}{\partial x_j} - \frac{\partial u_j}{\partial x_i} \right). \quad (11)$$

The stress term τ_{ij} is composed of a laminar and a turbulent component as

$$\tau_{ij} = \tau_{ij}^L + \tau_{ij}^T, \quad (12)$$

where

$$\tau_{ij}^L = -2\mu \left(S_{ij} - \frac{1}{3} \frac{\partial u_k}{\partial x_k} \delta_{ij} \right). \quad (13)$$

For linear eddy-viscosity models using the Boussinesq eddy viscosity assumption:

$$\tau_{ij}^T = \frac{2}{3} \rho K \delta_{ij} - 2\mu_t^* \left(S_{ij} - \frac{1}{3} \frac{\partial u_k}{\partial x_k} \delta_{ij} \right) \quad (14)$$

where μ_t^* is the turbulent eddy viscosity computed by a linear turbulence model. For the nonlinear eddy-viscosity models EASM-ko and EASM-ke:

$$\begin{aligned} \tau_{ij}^T = & \frac{2}{3} \rho K \delta_{ij} - 2\mu_t^* \left(S_{ij} - \frac{1}{3} \frac{\partial u_k}{\partial x_k} \delta_{ij} \right. \\ & + [a_2 a_4 (S_{ik} W_{kj} - W_{ik} S_{kj}) \\ & \left. - 2a_3 a_4 (S_{ik} S_{kj} - \frac{1}{3} S_{kl} S_{lk} \delta_{ij})] \right) \end{aligned} \quad (15)$$

where the terms a_2 , a_3 , and a_4 are defined in the next section.

In CFL3D, the kinetic energy of the fluctuating turbulent field K is ignored in the definition of p and E in equations (4) and (5). Furthermore, for all linear eddy-viscosity models, the term involving K is ignored in the definition of τ_{ij}^T in equation (14), and the ψ_j term in the energy equation (3) is assumed to be zero. These approximations and assumptions have relatively little effect for most flows at low or transonic Mach numbers, but could have significant impact for hypersonic flows. From a coding perspective, for linear eddy-viscosity models, the end result is that the laminar Navier-Stokes equations are identical to the turbulent Navier-Stokes equations with the exception that μ is replaced by $\mu + \mu_t^*$ and μ/Pr is replaced by $\mu/\text{Pr} + \mu_t^*/\text{Pr}_t$ (in these equations Pr is taken as 0.72 and Pr_t is taken as 0.9).

For the nonlinear models, the term involving K is included in the definition of τ_{ij}^T in equation (15), and the ψ_j term in the energy equation (3) is modeled via equation (9). However, K is still ignored in the definition of p and E in equations (4) and (5). Therefore, like the linear turbulence models, strictly speaking the nonlinear turbulence models are not applicable for

hypersonic flows either, as coded in CFL3D. From a coding perspective, the nonlinear models are similar to the linear models except that additional terms beside μ_t^* and μ_t^*/Pr_t must be added to the right-hand sides of the momentum and energy equations (2) and (3) when going from laminar to turbulent Navier-Stokes.

All the turbulence models in CFL3D, including EASM-ko and EASM-ke, are solved uncoupled from the mean flow equations using implicit approximate factorization. Their advective terms are solved using first-order upwind differencing. Details for obtaining the μ_t^* term for the EASM-ko and EASM-ke models are given in the next section.

3 THE EASM EXPLICIT ALGEBRAIC STRESS MODELS

For background and summary on the derivation of EASM, see Gatski and Speziale [3], Jongen and Gatski [14], Rumsey et al.[6], and Rumsey and Gatski [15]. The following section bypasses the derivation and jumps directly to the final resulting equations for the EASM-ko and EASM-ke models, and also outlines the method of solution in CFL3D.

The kinematic eddy viscosity μ_t^* is given by

$$\nu_t^* = \mu_t^*/\rho = C_\mu^* K \tau = -K \alpha_1, \quad (16)$$

with $\tau \equiv 1/\omega$ for EASM-ko and $\tau \equiv K/\varepsilon$ for EASM-ke. Thus, α_1/τ is equivalent to $-C_\mu^*$, which is variable (as opposed to constant as in most linear two-equation models). The nominal level for C_μ^* in a zero-pressure-gradient log layer is approximately 0.09. The value of α_1/τ is obtained from the solution to the following cubic equation at each point in the flow field:

$$\left(\frac{\alpha_1}{\tau}\right)^3 + p \left(\frac{\alpha_1}{\tau}\right)^2 + q \left(\frac{\alpha_1}{\tau}\right) + r = 0, \quad (17)$$

where

$$p = -\frac{\gamma_1^*}{\eta^2 \tau^2 \gamma_0^*} \quad (18)$$

$$q = \frac{1}{(2\eta^2 \tau^2 \gamma_0^*)^2} \left(\gamma_1^{*2} - 2\eta^2 \tau^2 \gamma_0^* a_1 - \frac{2}{3} \eta^2 \tau^2 a_3^2 + 2\mathcal{R}^2 \eta^2 \tau^2 a_2^2 \right) \quad (19)$$

$$r = \frac{\gamma_1^* a_1}{(2\eta^2 \tau^2 \gamma_0^*)^2}. \quad (20)$$

The correct root to choose from this equation is the root with the lowest real part [16]. Also, the degenerate case when $\eta^2 \rightarrow 0$ must be avoided. See Rumsey and Gatski [15] for further details. In the current implementation, the resulting $C_\mu^* = -(\alpha_1/\tau)$ is limited by $C_\mu^* = \max(-(\alpha_1/\tau), 0.0005)$. Other parameters are given by

$$\eta^2 \equiv \{\mathbf{S}^2\} = S_{ij} S_{ji} = S_{ij} S_{ij} \quad (21)$$

$$\{\mathbf{W}^2\} = W_{ij} W_{ji} = -W_{ij} W_{ij} \quad (22)$$

$$\mathcal{R}^2 = -\frac{\{\mathbf{W}^2\}}{\{\mathbf{S}^2\}} \quad (23)$$

$$a_1 = \frac{1}{2} \left(\frac{4}{3} - C_2 \right) \quad (24)$$

$$a_2 = \frac{1}{2} (2 - C_4) \quad (25)$$

$$a_3 = \frac{1}{2} (2 - C_3) \quad (26)$$

$$a_4 = \left[\gamma_1^* - 2\gamma_0^* \left(\frac{\alpha_1}{\tau} \right) \eta^2 \tau^2 \right]^{-1} \tau. \quad (27)$$

Also,

$$\gamma_0^* = C_1^1/2 \quad (28)$$

$$\gamma_1^* = \frac{1}{2} C_1^0 + \left(\frac{C_{\varepsilon 2} - C_{\varepsilon 1}}{C_{\varepsilon 1} - 1} \right) \quad (29)$$

and $C_{\varepsilon 1} = 1.44$, $C_{\varepsilon 2} = 1.83$, $C_1^0 = 3.4$, $C_1^1 = 1.8$, $C_2 = 0.36$, $C_3 = 1.25$, and $C_4 = 0.4$.

The preceding implementation is exactly the same for EASM-ko or EASM-ke. The two methods differ in the two equations solved (K - ω vs. K - ε). For EASM-ko, the explicit tensor representation for τ_{ij} is coupled with the following K - ω two-equation model:

$$\frac{DK}{Dt} = \mathcal{P} - f_{\beta^*} K \omega + \frac{\partial}{\partial x_k} \left[\left(\nu + \frac{\nu_t^*}{\sigma_K} \right) \frac{\partial K}{\partial x_k} \right] \quad (30)$$

$$\frac{D\omega}{Dt} = \gamma \frac{\omega}{K} \mathcal{P} - \beta \omega^2 + \frac{\partial}{\partial x_k} \left[\left(\nu + \frac{\nu_t^*}{\sigma_\omega} \right) \frac{\partial \omega}{\partial x_k} \right], \quad (31)$$

where

$$\mathcal{P} = -\tau_{ij} \frac{\partial u_i}{\partial x_j} \approx 2\nu_t^* \eta^2 \quad (32)$$

and $\sigma_K = 1$, $\sigma_\omega = \kappa^2 / [\sqrt{C_\mu} (\beta - \gamma)]$, $\kappa = 0.41$, $\gamma = 0.53$, $\beta = 0.83$, and $C_\mu = 0.0895$. Note that for 2-D incompressible flows, $\mathcal{P} = 2\nu_t^* \eta^2$ is exact. In CFL3D, the user has the option of using the exact or the approximate \mathcal{P} term. We have found there to be very little difference for a wide variety of subsonic and transonic 2-D aerodynamic-type flows, and use of the approximate term is more robust during transient stages of the computation in some cases. Except where otherwise noted, all the results in this paper were obtained using the approximate term.

Also, it should be noted that the values of σ_K and γ in this model are different than reported in Rumsey and Gatski [15]. They were changed recently to improve the model's capability for jet-type flows (see Georgiadis et al.[17]). The change was found to have relatively small impact for wall-bounded flows in general. In the current implementation, \mathcal{P} in the K -equation is limited to be less than 20 times the destruction term $f_{\beta^*} K \omega$. The function f_{β^*} , taken from from Wilcox [12], is given by

$$f_{\beta^*} = 1 \quad \text{when} \quad \chi_k \leq 0 \quad (33)$$

$$f_{\beta^*} = \frac{1 + 680\chi_k^2}{1 + 400\chi_k^2} \quad \text{when} \quad \chi_k > 0 \quad (34)$$

$$\chi_k = \frac{C_\mu^2}{\omega^3} \frac{\partial K}{\partial x_j} \frac{\partial \omega}{\partial x_j}, \quad (35)$$

where the C_μ^2 term in the formula for χ_k is necessary because ω in the current model does not "absorb" C_μ as in Wilcox's model.

For the EASM-ke two-equation model:

$$\frac{DK}{Dt} = \mathcal{P} - \varepsilon + \frac{\partial}{\partial x_k} \left[\left(\nu + \frac{\nu_t}{\sigma_K} \right) \frac{\partial K}{\partial x_k} \right] \quad (36)$$

$$\frac{D\varepsilon}{Dt} = C_{\varepsilon 1} \frac{\varepsilon}{K} \mathcal{P} - f_\varepsilon C_{\varepsilon 2} \frac{\varepsilon^2}{K} + \frac{\partial}{\partial x_k} \left[\left(\nu + \frac{\nu_t}{\sigma_\varepsilon} \right) \frac{\partial \varepsilon}{\partial x_k} \right], \quad (37)$$

where \mathcal{P} is given by equation (32) and is limited in the K -equation to be less than 20 times the destruction term ε . Also, $f_\varepsilon = [1 - \exp(-Re_K/10.8)]$, $Re_K = K^{1/2}d/\nu$, $\sigma_K = 1.0$, $\sigma_\varepsilon = \kappa^2/[\sqrt{C_\mu}(C_{\varepsilon 2} - C_{\varepsilon 1})]$, $C_{\varepsilon 1} = 1.44$, $C_{\varepsilon 2} = 1.83$, $C_\mu = 0.0885$, and d is the distance to the nearest wall. Additional wall damping functions (such as f_μ , to achieve expected asymptotic behavior of the turbulence quantities very near the wall) are not employed in the current EASM-ke model. Note that in equations (36) and (37), the diffusion terms are modeled using an *equilibrium* eddy viscosity $\nu_t = C_\mu K^2/\varepsilon$, where the constant $C_\mu = 0.0885$ for this model. This is different than in the EASM-ko model, which uses the *actual* eddy viscosity ν_t^* (with variable C_μ^*) in its modeled diffusion terms. The diffusion terms for both EASM-ko and EASM-ke are approximate models in any case; see, for example, Warsi [18].

In CFL3D, the turbulence equations are nondimensionalized by the same reference variables as the Navier-Stokes equations: a_{ref} , ρ_{ref} , μ_{ref} , and L_{ref} , where a is speed of sound, ρ is density, μ is molecular viscosity, and L is length scale corresponding to unit one of the computational grid. Thus, denoting nondimensional variables with a tilde: $\tilde{K} = K/(a_{\text{ref}}^2)$, $\tilde{\omega} = (\mu_{\text{ref}}\omega)/(\rho_{\text{ref}}a_{\text{ref}}^2)$, and $\tilde{\varepsilon} = (\mu_{\text{ref}}\varepsilon)/(\rho_{\text{ref}}a_{\text{ref}}^4)$.

The turbulent boundary conditions applied at solid walls are $K_w = 0$, $\varepsilon_w = 2\nu_w(\partial\sqrt{K}/\partial n)_w^2$, and $\omega_w = 10(6\nu_w)/[\beta(\Delta n)^2]$, where Δn is the distance to the first cell center away from the wall. The boundary condition for ω_w is from Menter [19]. This boundary condition simulates the analytical behavior of ω near solid walls without the need for specifying the solution at interior points. At farfield inflow boundaries, the following nondimensional values are assigned as freestream reference values in CFL3D: $\tilde{K} = 9 \times 10^{-9}$ and $\tilde{\omega} = 9 \times 10^{-8}$ for EASM-ko; and $\tilde{K} = 1 \times 10^{-9}$ and $\tilde{\varepsilon} = 1 \times 10^{-17}$ for EASM-ke. The end result for both models is that nondimensional $\tilde{\mu}_t = \mu_t/\mu_{\text{ref}} \approx 0.009$ at farfield inflow boundaries (based on $C_\mu^* = 0.09$, which is only approximate because C_μ^* is variable in these models). At outflow boundaries, the turbulent quantities are extrapolated from the interior of the computational domain.

Some additional details concerning the method for solving the two-equation turbulence models are now given. First, the following is an example showing the transformation from Cartesian coordinates to generalized coordinates:

$$u_j \frac{\partial k}{\partial x_j} = U \frac{\partial k}{\partial \xi} + V \frac{\partial k}{\partial \eta} + W \frac{\partial k}{\partial \zeta}, \quad (38)$$

where

$$U = \xi_x u + \xi_y v + \xi_z w + \xi_t \quad (39)$$

$$V = \eta_x u + \eta_y v + \eta_z w + \eta_t \quad (40)$$

$$W = \zeta_x u + \zeta_y v + \zeta_z w + \zeta_t \quad (41)$$

and ξ , η , and ζ are the three generalized coordinate directions. When transforming into generalized coordinates, cross-derivative terms are neglected in the diffusion-type terms that appear in the turbulence equations.

The two turbulence equations are solved decoupled using implicit approximate factorization. Each sweep requires the solution of a scalar tridiagonal matrix. The production terms are treated explicitly, lagged in time, while the destruction and diffusion terms are treated implicitly. It should be noted here that in CFL3D, the K , ω , and ε terms are not allowed to go negative during the solution procedure. If the update yields a negative result, it is instead limited to a very small positive number, and a counter keeps track of the number of times this occurs in the flowfield as an indicator of non-convergence in the solution. Furthermore, τ_{11} , τ_{22} , and τ_{33} are limited to be positive (this is the realizability constraint). In EASM-ke, $\eta^2\tau^2$ and $\mathcal{R}^2\eta^2\tau^2$ are each limited to be less than 1200 in magnitude. In both EASM-ko and EASM-ke, where ω or ε appears in the denominator of equation (15) (i.e., in the nonlinear terms added to the Navier-Stokes equations), these values are limited to be greater than or equal to their freestream reference levels in order to avoid dividing by unrealistically small numbers during the convergence process.

4 VALIDATION TEST CASES

This section contains a detailed account of a series of validation test cases to which the EASM-ko and EASM-ke models have been applied. The first 7 cases are also “standard” CFL3D test cases, described and available on the CFL3D website [20]. (In some instances, the case on the website has been set up for a different turbulence model other than EASM-ko or EASM-ke, and some adjustments to CFL number are necessary in the provided input file in order to get the cases to run.) The last 2 cases are not currently available on the website. For the first case (flat plate), grid sensitivity studies are described in this report. All of the subsequent cases use only a single grid size, with no parametric variations performed. However, many of the grids used in these validations were found to be fine enough to capture the flow features of interest in previous grid sensitivity studies performed by the authors or by other researchers. In each case, the boundary conditions are described in detail; unless otherwise noted, at all solid walls a no-slip, adiabatic wall boundary condition is used. At these walls, the turbulence boundary conditions are those described in section 3. For the mean flow variables, velocity components at the wall are set to zero, $\partial T_w/\partial n = 0$, and p_w is determined using linear extrapolation from the interior of the domain. Note that the EASM-ke model sometimes has difficulty establishing turbulence when started from freestream or weak turbulence initial conditions. Therefore, for all the results in this paper, EASM-ke was initialized from the corresponding EASM-ko solution.

4.1 Flat Plate

The flat plate case (zero pressure gradient) was performed at $M = 0.3$, $Re = 6 \times 10^6$ per unit length of the grid. The default grid size for this case was 65×97 . Fig. 1 shows a picture of the grid. The viscous, adiabatic wall was unit one in length. Symmetry boundary conditions were imposed on a region of length $x = 0.333$ in front of the plate. Grid domain height was approximately 1.0, minimum normal grid spacing at the wall was 1×10^{-6} , and the grid was stretched at a rate of 1.18 until the vertical spacing first exceeded the horizontal spacing. Horizontal grid spacing was constant at $\Delta x = 0.0208333$.

At the inflow boundary, the total pressure and total temperature were set via $p_T/p_{\text{ref}} = 1.02828$ and $T_T/T_{\text{ref}} = 1.0080$, and a 1-D characteristic boundary condition was used to determine the other flow variables [9]. At the outflow boundary, linear extrapolation was employed. At the top boundary, a farfield Riemann-invariant 1-D characteristic boundary condition was employed.

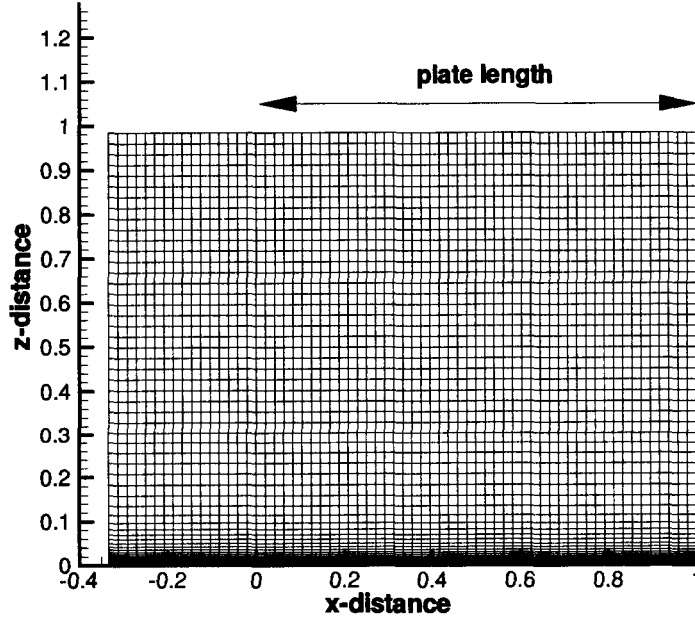


Figure 1: Flat plate grid, 65×97 .

Surface skin friction coefficient results using EASM-ko are shown in Fig. 2 for a grid density study. A total of four grids were used: each had 65 points in the streamwise direction, and the number of points in the normal direction was successively halved from 193 to 97 to 49 to 25. Thus, the default grid size (65×97) was included as well as one level finer and two levels coarser. Also shown in the figure are symbols giving three different theoretical curves from White [21], indicative of the type of spread that might be expected from experimental data of a turbulent flat plate boundary layer. As the grid is refined, the results approach the range defined by the theoretical curves. Looking at one particular x -location on the plate ($x = 0.8125$), and using second-order Richardson extrapolation on the finest two grids, one finds that the 65×193 grid yields a skin friction value 0.5% in error from the result on an infinitely-refined grid at this location. The default 65×97 grid is 2.0% in error, the 65×49 grid is 4.7% in error, and the 65×25 grid is 10.6% in error.

The same grid study was also conducted for EASM-ke. Results are shown in Fig. 3. Unlike EASM-ko, with EASM-ke the skin friction decreases with increasing grid density. In this case the 65×193 grid yields a skin friction value 0.1% in error from the result on an infinitely-refined grid at $x = 0.8125$. The default 65×97 grid is 0.6% in error, the 65×49 grid is 2.9% in error, and the 65×25 grid is 9.0% in error. Notice that the infinitely-refined skin friction levels approached by EASM-ke are slightly lower than those using EASM-ko.

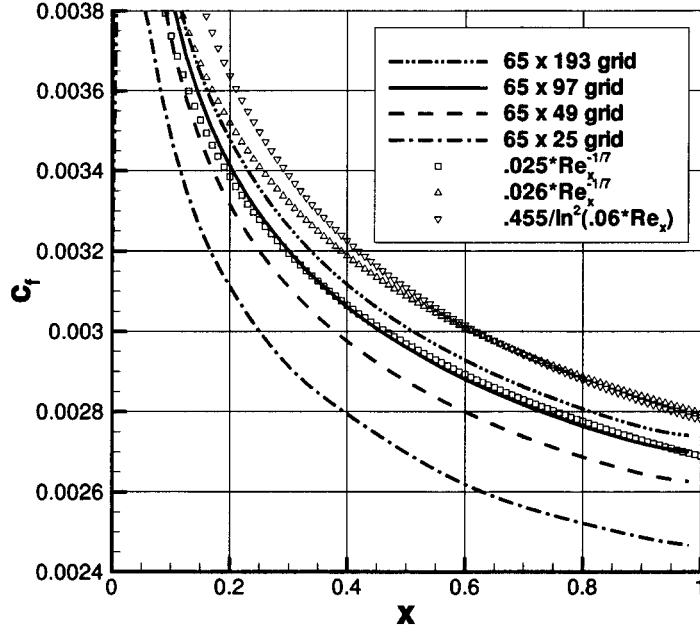


Figure 2: Effect of grid size normal to the wall on surface skin friction, EASM-ko.

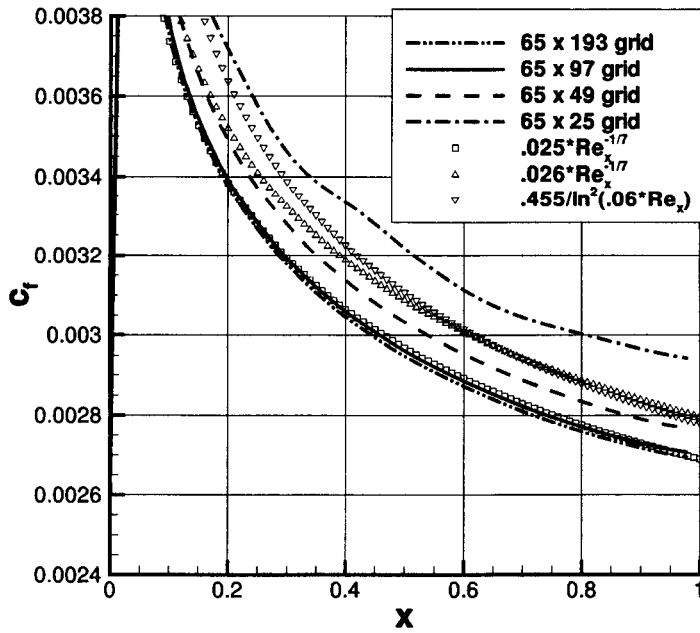


Figure 3: Effect of grid size normal to the wall on surface skin friction, EASM-ke.

Figs. 4 and 5 show the effect of varying the minimum normal spacing at the wall using EASM-ko and EASM-ke, while keeping grid size constant (at 65×97). The “standard” minimum spacing of 1×10^{-6} corresponds with an average y^+ value for the first cell-center off the wall of approximately 0.2. The minimum normal spacing was decreased to 1×10^{-7} (average y^+ of 0.02) as well as increased to 2.2×10^{-6} (average y^+ of 0.5), 5×10^{-6} (average y^+ of 1.1), and 1×10^{-5} (average y^+ of 2.2). In each case the stretching rate was varied to keep the grid height approximately 1.0. As the average y^+ level decreases, the skin friction increases for EASM-ko and decreases for EASM-ke. Using the result at $x = 0.8125$, the difference between the smallest y^+ and the largest y^+ tested is approximately 5% for EASM-ko and 2.6% for EASM-ke. The difference between using y^+ of 0.02 and 0.2 is only 0.3% for EASM-ko and less than 0.1% for EASM-ke.

A plot of u^+ vs. $\log(y^+)$ is shown for the two models in Fig. 6 using the 65×97 grid, along with Spalding theory from White [21]. Results agree well with the law-of-the-wall.

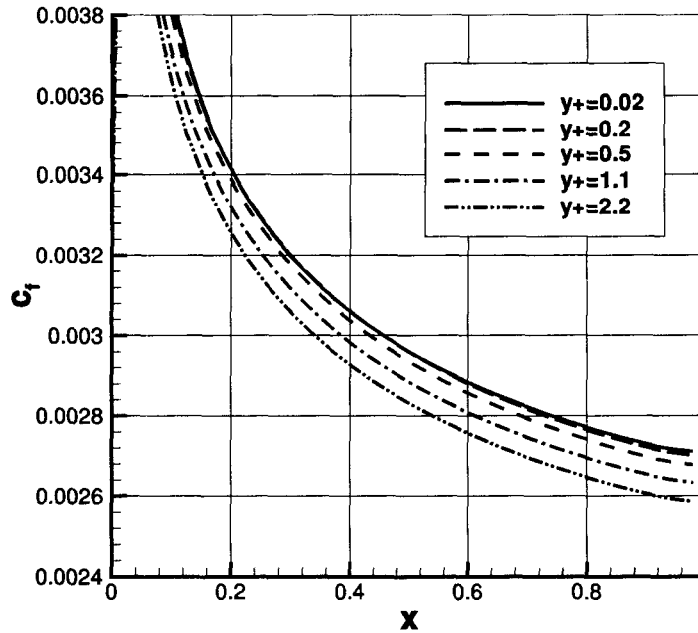


Figure 4: Effect of average minimum y^+ on surface skin friction, EASM-ko, 65×97 grid.

4.2 Back Step

The back step case compares against experimental data from Driver and Seegmiller [22]. In the experiment, several different upper wall angles were tested, but in the present computation, the upper wall was straight (0 deg). The test conditions were $M = 0.128$, $Re = 37573$ per unit step height H . In the grid for this configuration, the lower wall starts out at a height of 1.0, then drops to a height of 0.0 at $x/H = 0$. The upper wall is at a height of 9.0. The grid extends from $x/H = -4.0$ upstream to $x/H = 35$ downstream.

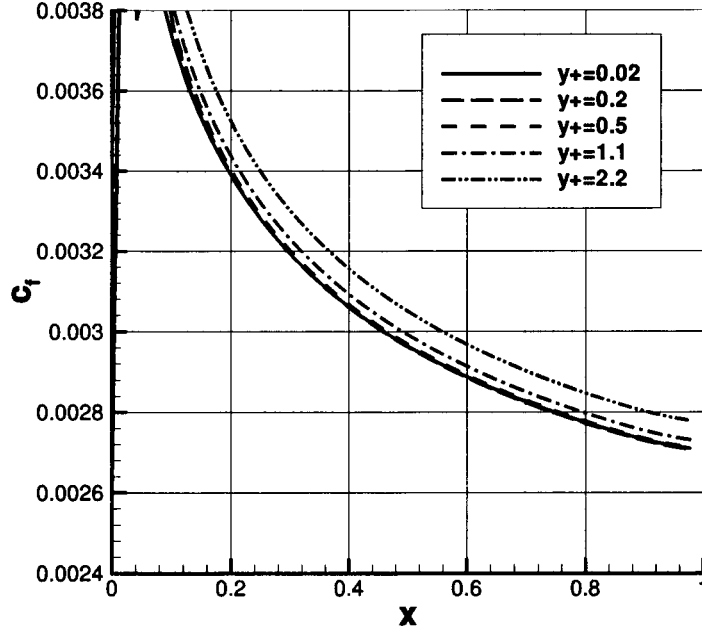


Figure 5: Effect of average minimum y^+ on surface skin friction, EASM-ke, 65×97 grid.

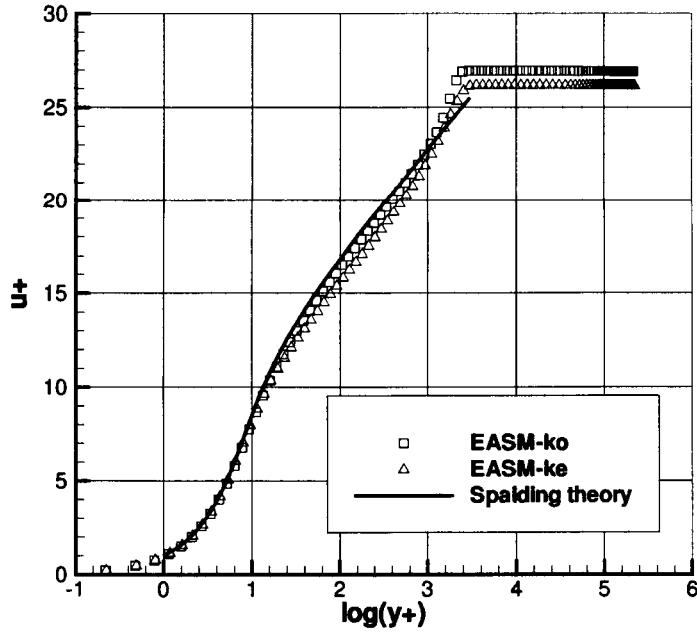


Figure 6: Velocity profiles for both models in wall variables at $x = 0.8$, 65×97 grid, $y^+=0.2$.

The grid itself is made up of two zones: 25×65 and 129×113 . These two zones abut along $x = 0$ in a patched-grid (non 1-to-1) fashion. Interpolation is used in CFL3D at the patched interface to provide communication between the zones. The minimum normal spacing at the walls varies within the range of approximately 0.006–0.007, which yields an average y^+ value at the first cell center off the walls of between 0.6 and 0.9. The only exception to this is the back face of the step itself, which has a normal spacing of 0.1. The streamwise grid spacing varies. It is clustered near the step, and stretched as it approaches the upstream and downstream boundaries. Two pictures of the grid are given in Figs. 7 and 8.

The lower wall, upper wall, and back of the step used viscous, adiabatic boundary conditions. At the upstream boundary, the density, velocity, and turbulence quantities were set to closely match experiment (see Rumsey et al.[6] for details concerning this procedure). The pressure at the inflow was extrapolated from the interior of the domain. At the downstream boundary, the pressure was set to $p/p_{\text{ref}} = 1.00149$ and all other quantities were extrapolated from the interior of the domain.

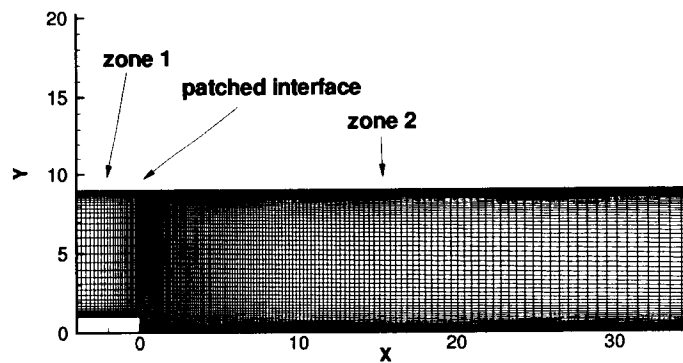


Figure 7: Backstep grid, 25×65 and 129×113 .

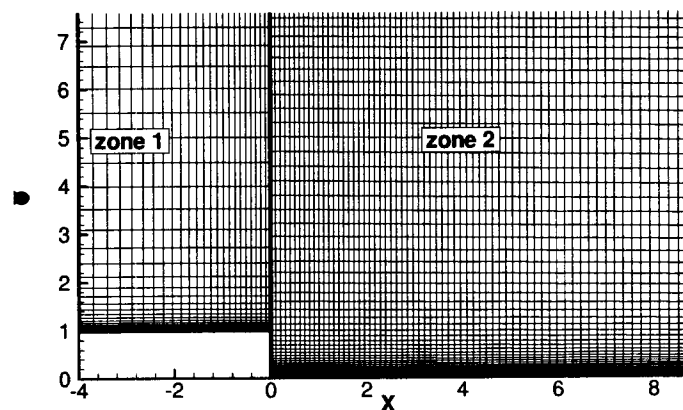


Figure 8: Close-up of the backstep grid near the interface between zones.

Lower wall pressure coefficient and skin friction coefficient for both EASM-ko and EASM-ke are given in Figs. 9 and 10. A series of velocity profiles is given in Figs. 11, 12, and 13, and turbulent shear stress is given in Figs. 14, 15, and 16.

Reattachment length in the experiment was approximately in the range of $x = 6 - 6.3$. Using EASM-ko, the computed reattachment length was $x = 6.30$, whereas for EASM-ke it was $x = 5.86$. Both of these are in very good agreement with the experiment, considering that many turbulence models have been shown to seriously underpredict reattachment length by 30% or more [22]. The EASM-ko skin friction results agree extremely well with experiment in general, but EASM-ke underpredicts the levels in the separated region and overpredicts the levels after reattachment. This poorer prediction of EASM-ke is consistent with skin friction results that others have found for this case using different $k-\varepsilon$ models (see, e.g., Menter [19]). Velocity profiles for both models are similar. Both do a reasonably good job in the separated region, but then do not predict as rapid a recovery after reattachment as experiment. This too-slow recovery from separation is a chronic problem with almost all RANS turbulence models in use today [23]. Turbulent shear stress is predicted well by both models up through $x = 2.5$, but then the peak shear is underpredicted (and is also farther from the wall) through approximately $x = 5.5$. Downstream of this, the levels and shapes again agree fairly well with experiment.

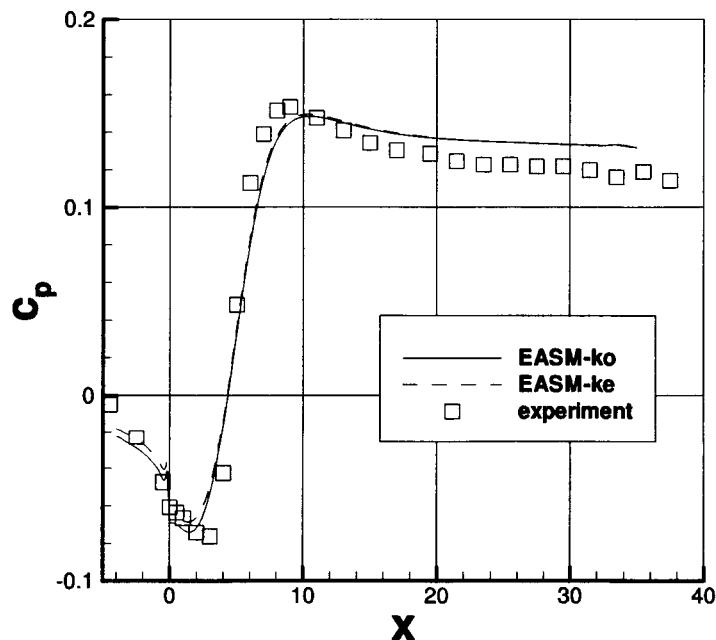


Figure 9: Backstep surface pressure coefficients.

4.3 Transonic Diffuser

This case models the strong-shock diffuser experiment of Sajben and Kroutil [24]. Fig. 17 shows the 81×51 grid, which was obtained from the NPARC Alliance Validation Archive website [25].

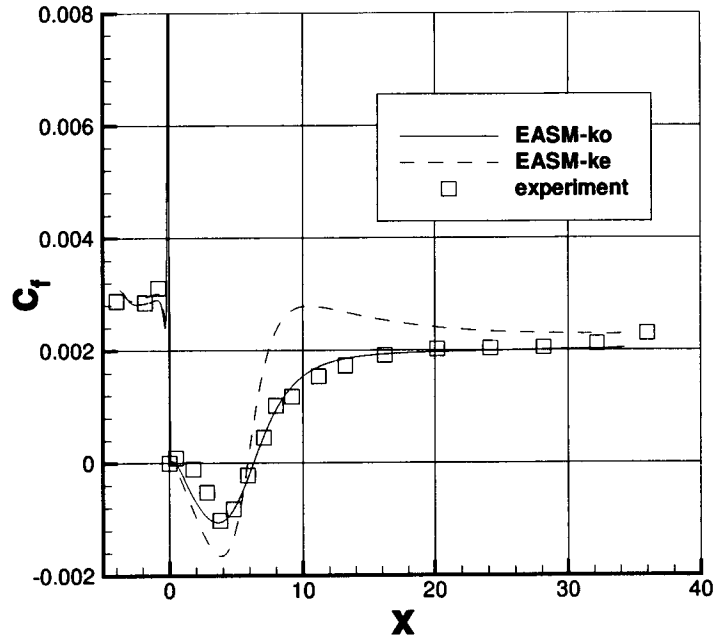


Figure 10: Backstep surface skin friction coefficients.

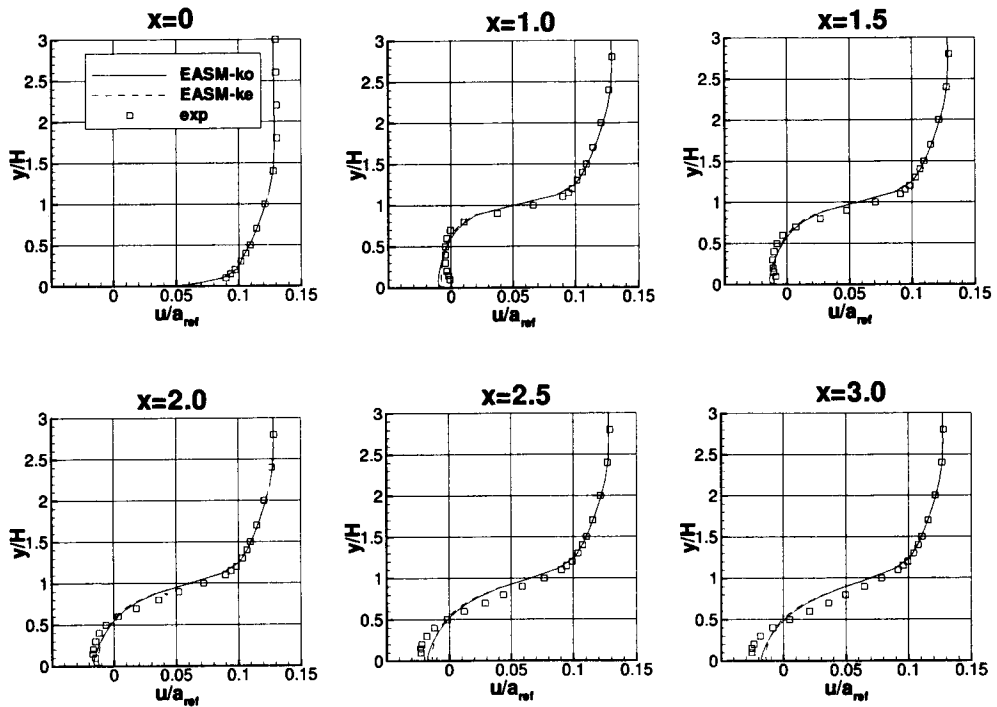


Figure 11: Backstep velocity profiles, set 1.

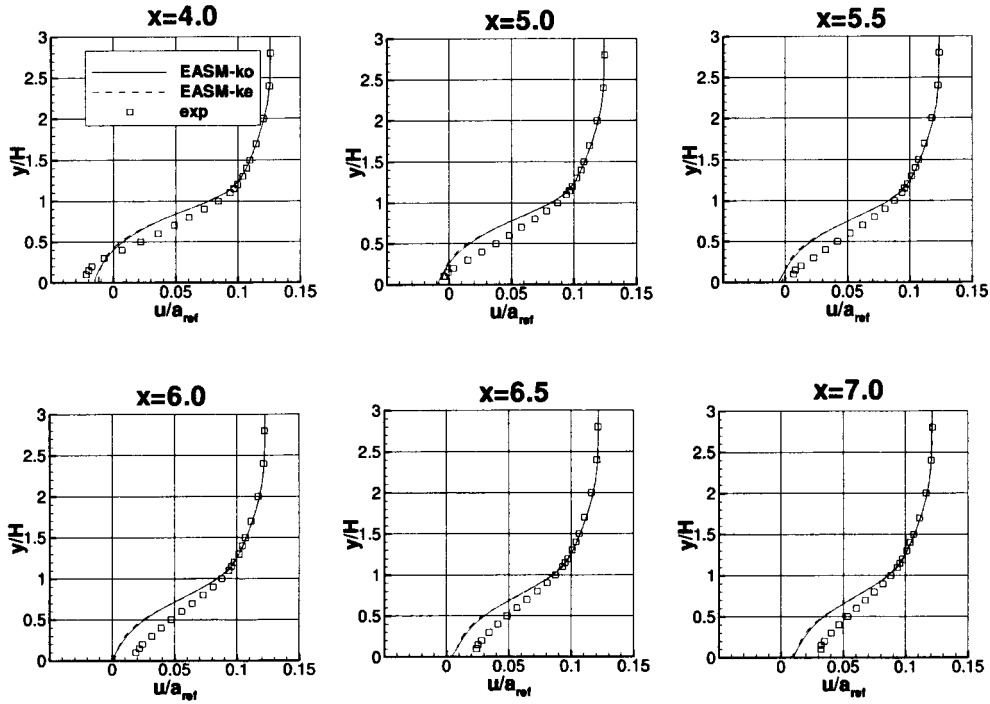


Figure 12: Backstep velocity profiles, set 2.

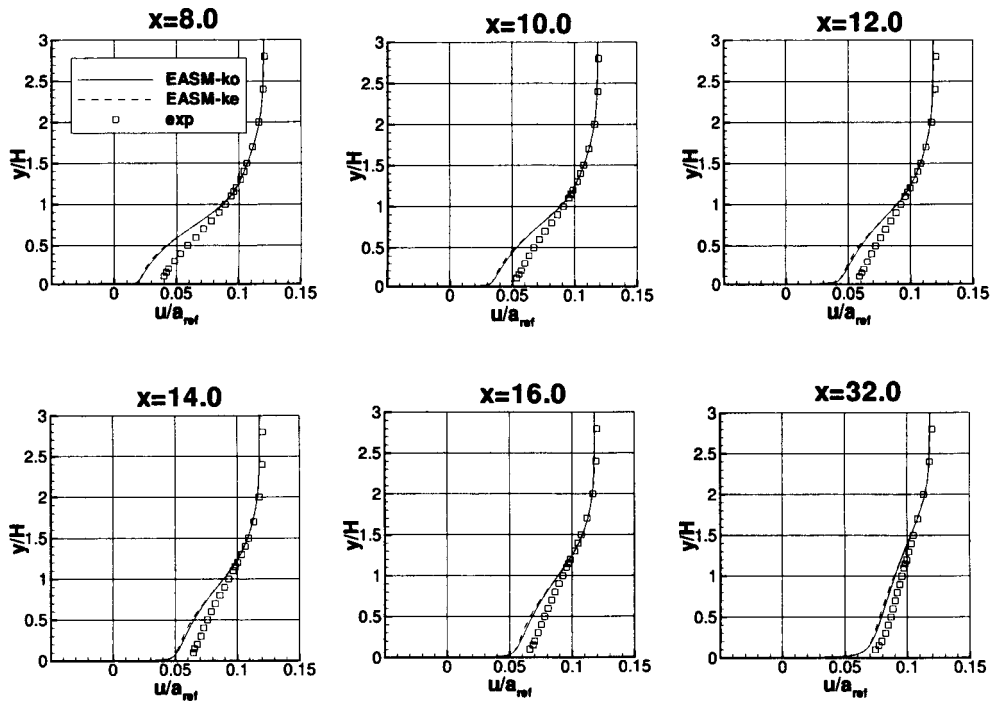


Figure 13: Backstep velocity profiles, set 3.

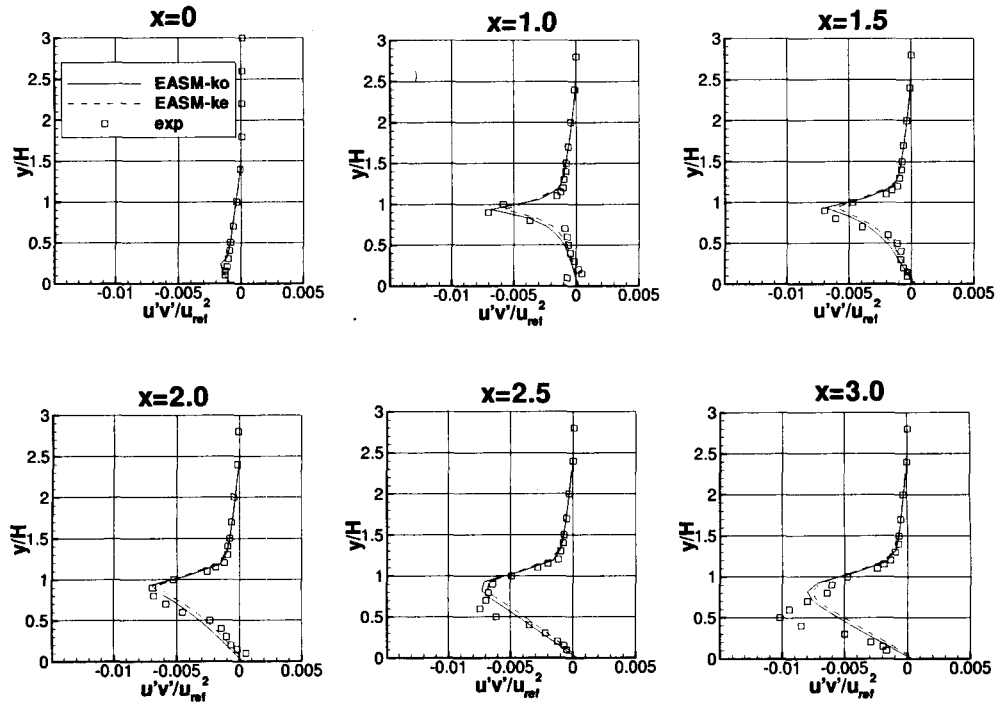


Figure 14: Backstep turbulent shear stress profiles, set 1.

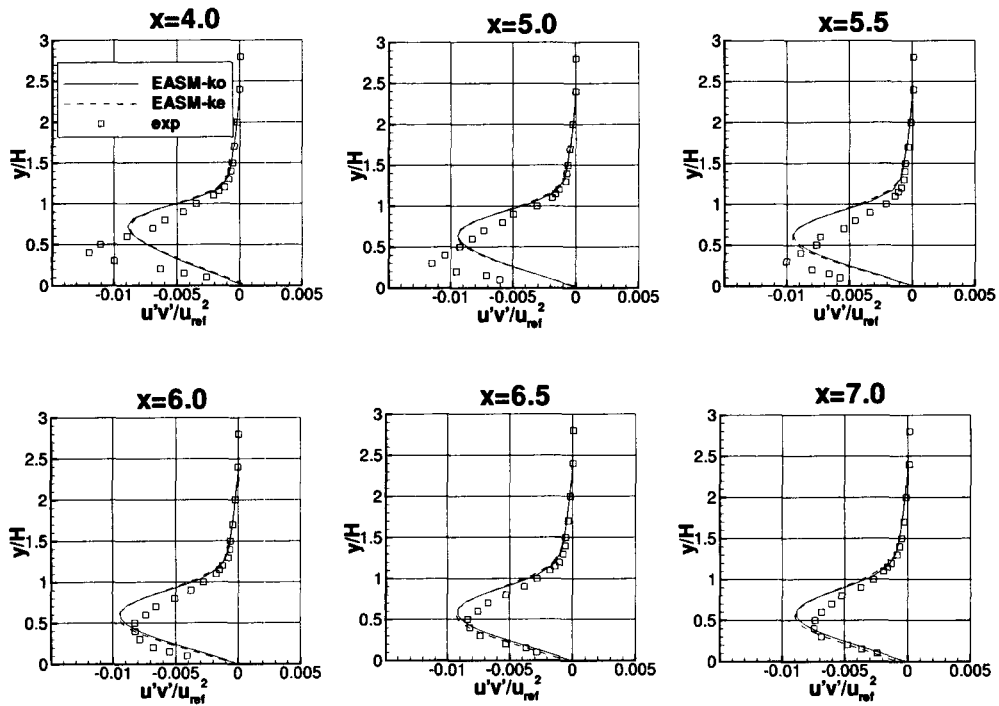


Figure 15: Backstep turbulent shear stress profiles, set 2.

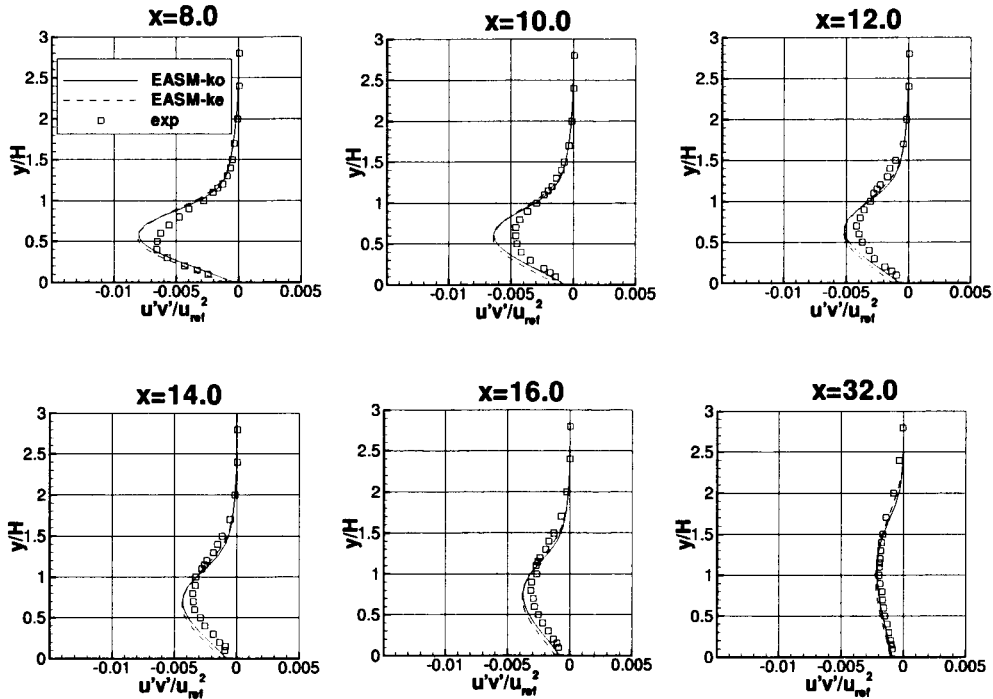


Figure 16: Backstep turbulent shear stress profiles, set 3.

This configuration had an entrance to throat area ratio of 1.4 and an exit to throat area ratio of 1.5. This flow is characterized by the ratio, R , of exit static to inflow total pressure. For the strong-shock case R is 0.72. In the strong shock case, there is separated flow on the upper wall downstream of the shock wave [25]. The grid had a minimum spacing at the walls of approximately 0.0001, yielding an average minimum y^+ value at the first cell center off the wall of approximately 2.5.

When computing this case in CFL3D, the lower and upper walls were modeled as viscous, adiabatic walls. At the inflow plane, the total pressure divided by reference pressure was 1.894 and total temperature divided by reference temperature was 1.201. At the outflow plane, the static pressure divided by reference pressure was 1.364. Reference conditions (at the throat) were: $M=1.0$ and $Re=937,000$ per throat width. (In the grid, the throat width was unit 1.)

Computed wall pressures are shown compared to experiment in Figs. 18 and 19 for the lower and upper walls, respectively. There is a slight difference in predicted shock position, with EASM-ko downstream of EASM-ke, but both models agree well with experiment in general. Velocity profiles at four x -locations are shown in Fig. 20. Both EASM-ko and EASM-ke yield similar results in good agreement with experiment. Both models also correctly predict separated flow on the upper wall at the two stations $x/H=2.662$ and 4.611 , although in both cases the maximum reverse flow velocity magnitude is lower than in the experiment.

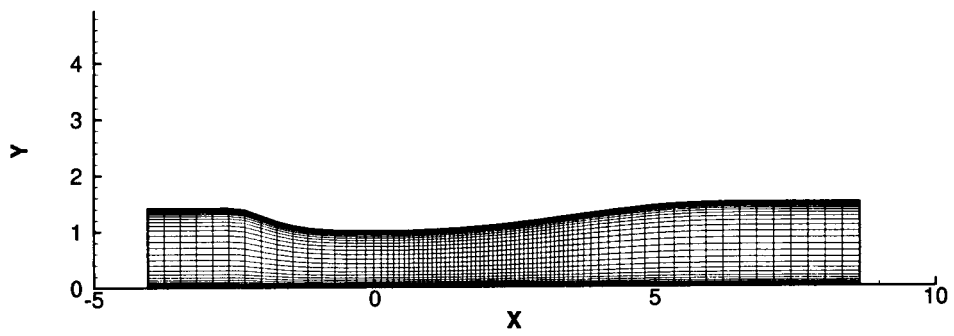


Figure 17: Transonic diffuser grid, 81×51 .

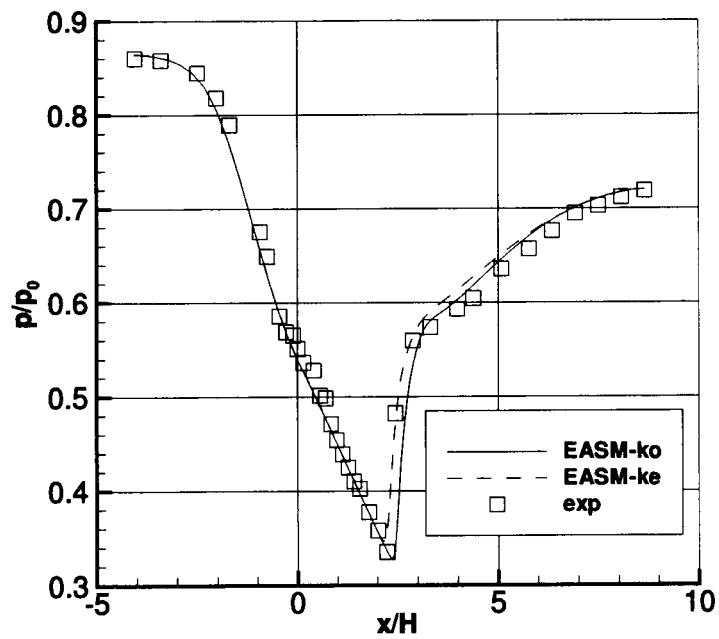


Figure 18: Transonic diffuser lower wall pressures.

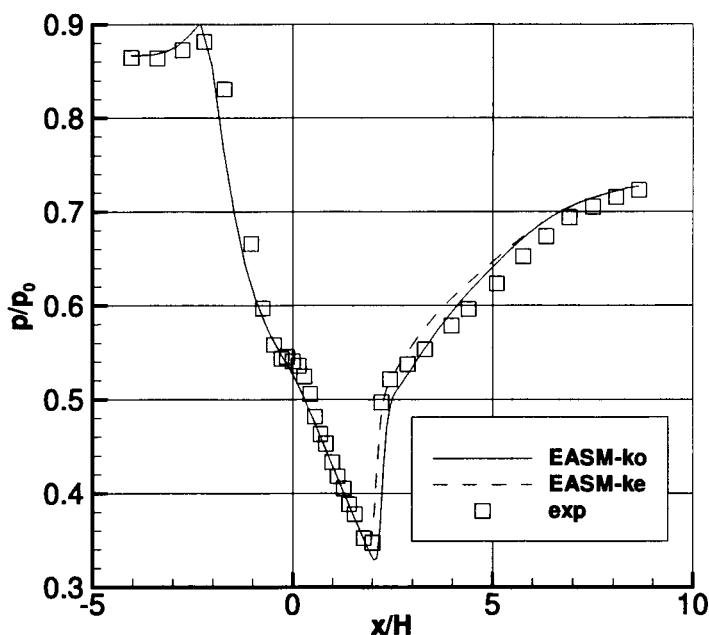


Figure 19: Transonic diffuser upper wall pressures.

4.4 NACA 4412 Airfoil

This case models the separated flow over a NACA 4412 airfoil, and compares with the experiment of Coles and Wadcock [26]. This flow was modeled computationally using a freestream Mach number of $M = 0.2$, Reynolds number $Re = 1.52 \times 10^6$ based on chord, and angle of attack of $\alpha = 13.87^\circ$. This flow separates on the rear part of the airfoil upper surface at these conditions. Fig. 21 shows a picture of the 257×81 grid used. The grid had a minimum spacing at the wall of 2×10^{-5} chords, a farfield extent of approximately 17 - 20 chords, and a total of 177 points on the airfoil surface. The average minimum $y+$ value of the first cell center off the wall was less than 2 for this grid.

Surface pressure coefficients are shown in Fig. 22 and upper surface velocity profiles are shown in Fig. 23. Both turbulence models predict similar surface pressures, which are in good agreement with experiment everywhere except near the upper surface trailing edge. For velocity profiles, EASM-ko yields results in excellent agreement with experiment, whereas EASM-ke predicts velocity levels that are too low (the profile has greater inflection). However, both models predict separation at the same location of $x/c = 0.830$.

Part of the reason for the poorer prediction of EASM-ke may be due to the fact that the $K-\epsilon$ formulation in general does not handle wall-bounded adverse pressure gradients well, because of shortcomings in the ϵ equation. See, for example, Rumsey and Gatski [15], Wilcox [12], and Rodi and Scheuerer [27]. Rodi and Scheuerer concluded that the generation term of the ϵ equation has to be increased above its usual level. Fig. 24 shows a plot of the predicted velocities in wall variables as compared to Spalding theory at $x/c = 0.5$ on the upper surface

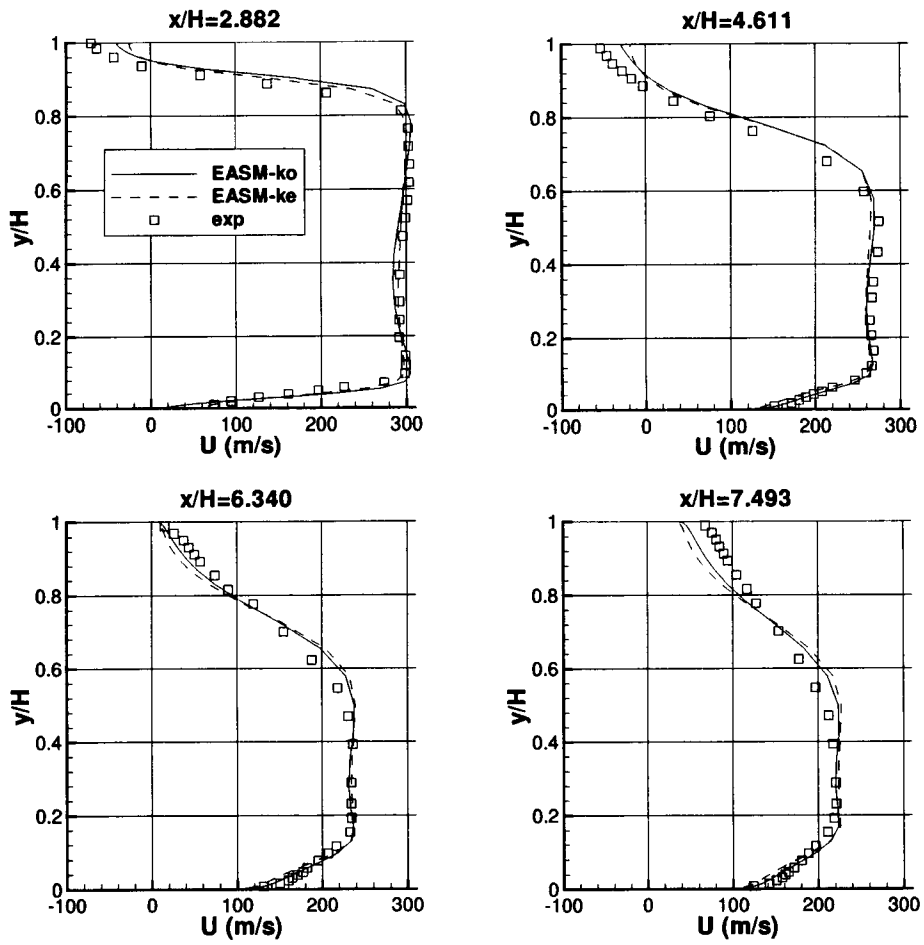


Figure 20: Transonic diffuser velocity profiles.

of the NACA 4412 airfoil. EASM-ke did not obtain the correct slope of the log layer in this adverse pressure gradient part of the flow, whereas EASM-ko did. This same problem was also shown and discussed in Rumsey and Gatski [15] and Nagano and Tagawa [28].

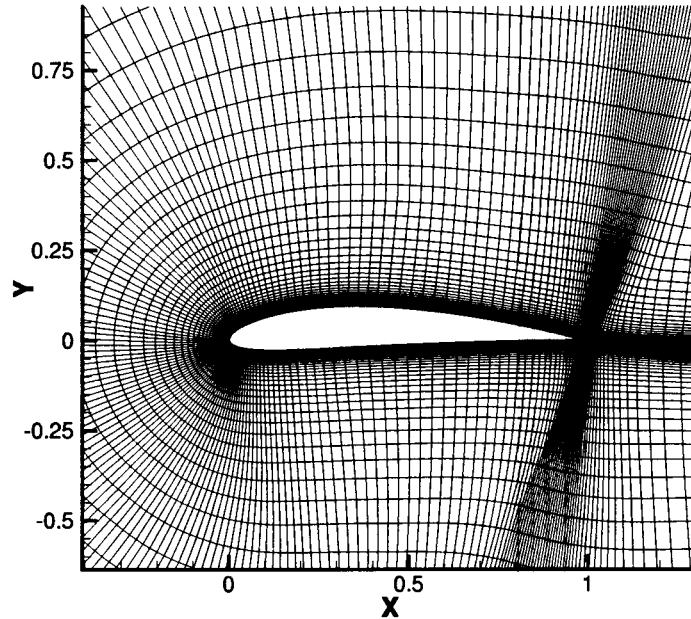


Figure 21: NACA 4412 grid, 257×81 .

4.5 Ejector Nozzle

The ejector nozzle case models a subsonic 2-D jet flow that entrains and mixes with a secondary outer flow. The experimental data are from Gilbert and Hill [29]. See also Georgiadis et al.[30].

This case has nozzle total pressure divided by atmospheric static pressure of 2.44, with total temperature = 644 R. The secondary flow has a total pressure equal to atmospheric and a temperature of 550 R. At the outflow used by this grid, the static pressure divided by the atmospheric static pressure was taken to be 0.9131. However, in CFL3D, a reference condition was chosen that corresponded with a non-zero Mach number: in this case it was taken to be $M=0.22$, which is the approximate Mach number at the secondary flow inlet in this grid. (Corresponding Reynolds number was taken to be approximately 1.64 million per foot.) Using $M=0.22$ and isentropic relations, total pressure divided by reference pressure is 1.0343 and total temperature divided by reference temperature is 1.0097. These numbers are used as inflow conditions for the secondary flow. Also as a result of choosing this reference condition, static pressure divided by reference pressure at the outflow is 0.9444. At the nozzle inlet, total pressure divided by reference pressure is 2.5237 and total temperature divided by reference temperature is 1.1822.

The grid consists of three zones with the following dimensions: 31×41 for primary nozzle,

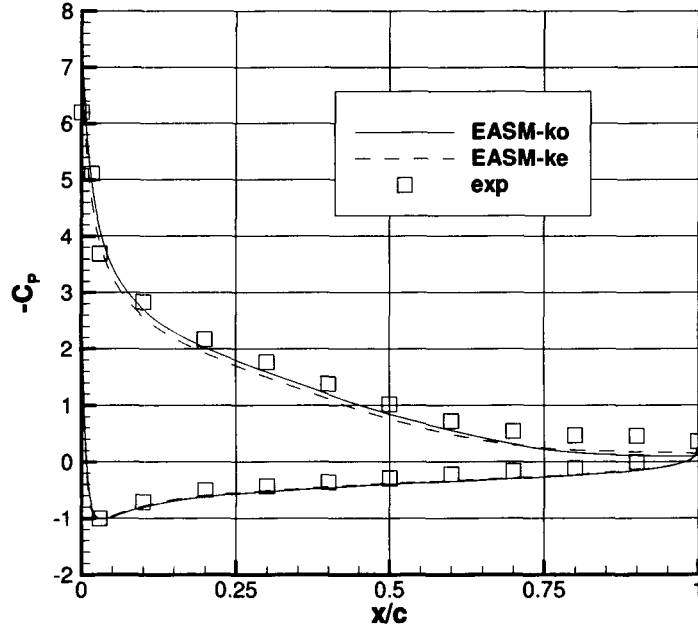


Figure 22: Surface pressure coefficient for NACA 4412.

31×71 for secondary inlet, and 101×121 for downstream. The grid is shown in Fig. 25. Minimum grid normal spacing at the walls yielded an average y^+ level of approximately 0.7.

Fig. 26 shows velocity profiles at four stations downstream using EASM-ko and EASM-ke. Both models overpredict the centerline velocity at the upstream stations and somewhat underpredict the jet width in general, but qualitatively the overall agreement is good (it is similar to results on the same grid using different turbulence models and a different code in Georgiadis et al.[30]).

4.6 Axisymmetric Bump

The axisymmetric bump case has served as a standard test case for transonic separated flow for many years. The experimental data are from Bachalo and Johnson [31], and have been used, for example, to validate Menter's widely-used SST turbulence model [32].

In this case, a turbulent boundary layer develops in the axial direction over an axisymmetric circular bump (smoothed at its leading and trailing edges). Wall effects in the experiment are minimal because the body does not generate any lift. For the particular case studied here, the Mach number is 0.875 and Reynolds number based on the length of the bump is 2.66×10^6 . At these conditions, there is a shock wave and the flow separates on the rear part of the bump, then reattaches a short distance downstream.

This case is run in "3-D mode" in CFL3D on a grid with two planes separated by 1.0 degrees, and with periodic boundary conditions used on each of the two circumferential planes. Fig. 27 shows a picture of one plane of the $181 \times 101 \times 2$ grid. The grid had an approximate minimum

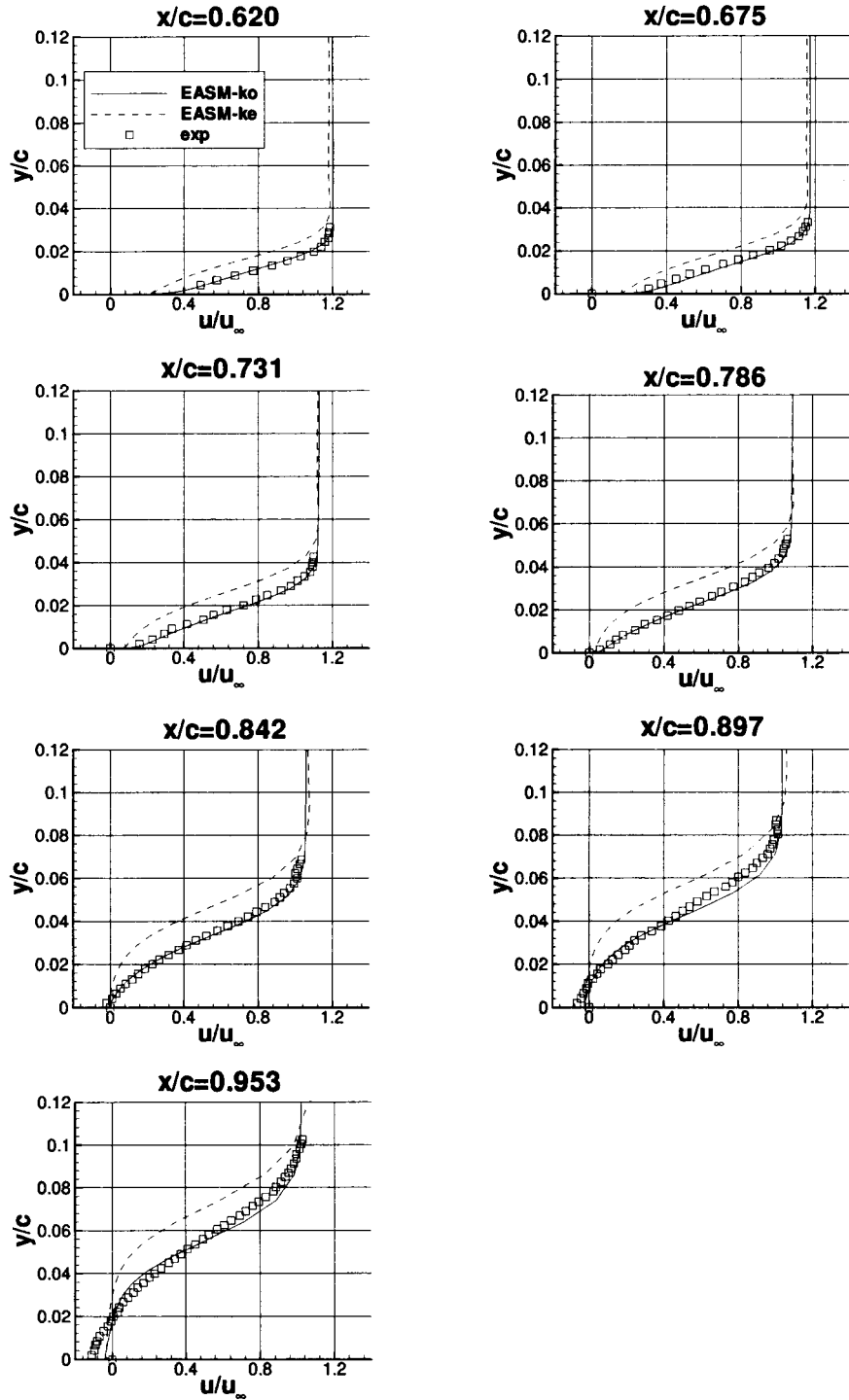


Figure 23: Velocity profiles for NACA 4412.

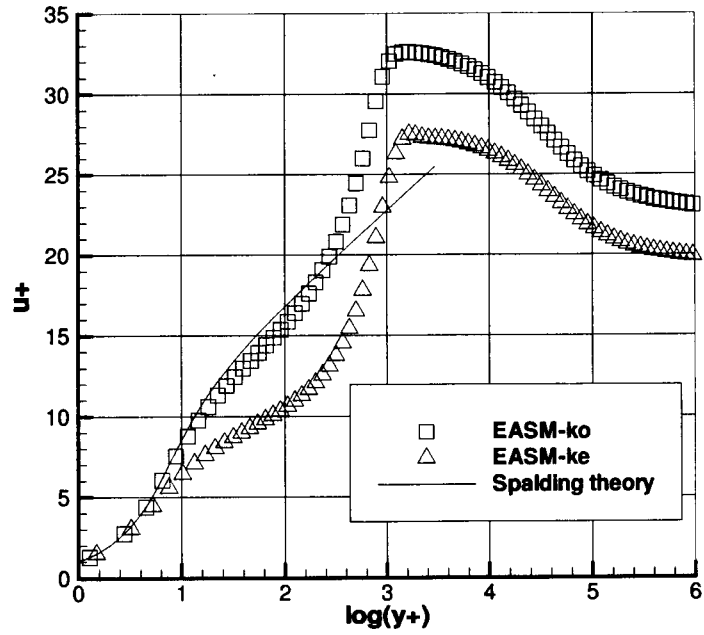


Figure 24: Velocity profiles in wall variables for upper surface of NACA 4412 at $x/c = 0.5$.

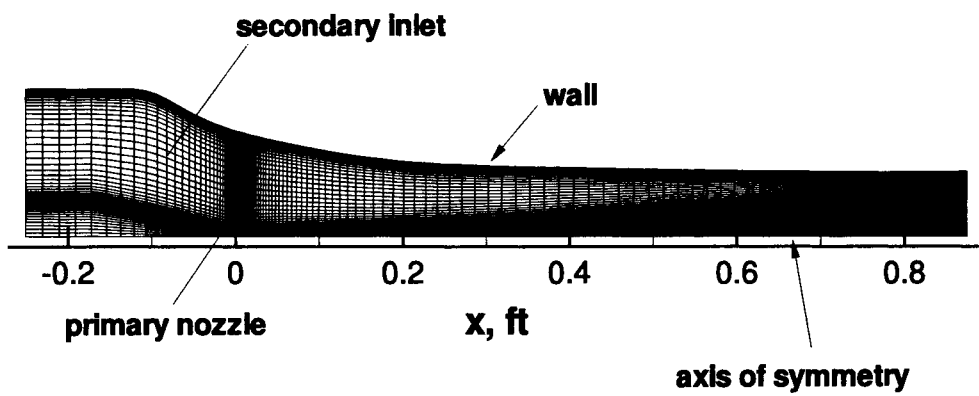


Figure 25: Ejector nozzle grid.

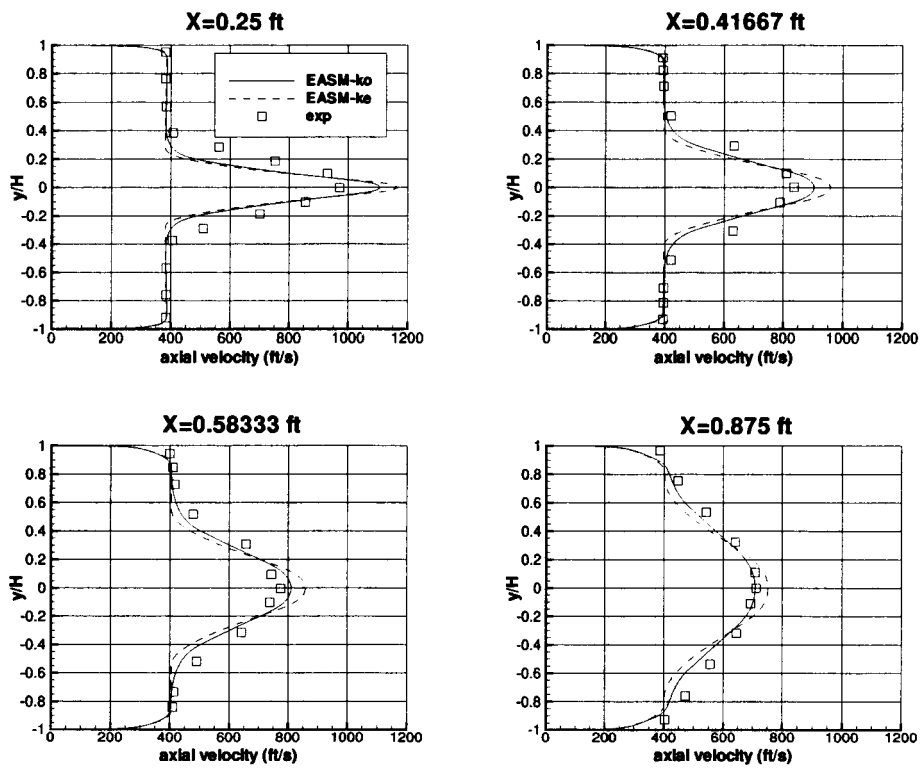


Figure 26: Jet velocity profiles for ejector nozzle.

spacing at the wall of 1.5×10^{-5} chords. Its farfield extent was 3.2 chords in front of the bump leading edge, 3.4 chords downstream of the bump trailing edge, and 4.1 chords domain height. There were 85 axial points on the bump part of the wall surface. The average minimum y^+ value of the first cell center off the wall was approximately 1.3 for this grid. Farfield-type boundary conditions were used on the upstream, downstream, and top faces of the grid.

Fig. 28 shows surface pressure coefficients on the body. Both EASM-ko and EASM-ke capture the shock position very accurately, as well as the shape of the pressure variation downstream. EASM-ke predicts the shock location slightly further forward. Velocity profiles and turbulent shear stress profiles at seven stations are shown in Figs. 29 and 30, respectively. At the station $x/c = 0.688$ upstream of separation, velocity profiles using EASM-ke agree with the experimental data somewhat better than EASM-ko, but EASM-ko recovers better than EASM-ke at the last three stations, downstream of reattachment. Both models yield excellent velocity profile results in the separated region. Also, both models predict turbulent shear stress profiles in reasonable agreement with experiment, with EASM-ke tending to give slightly lower peak levels in magnitude in the separated region.

In section 3, the use of an approximate production term in the EASM-ko and EASM-ke models was discussed, and it was asserted that use of the approximate term makes very little difference for a wide variety of subsonic and transonic 2-D aerodynamic-type flows. In fig. 31, shear stress profiles at two stations are shown using the two models with both the approximate \mathcal{P} term as well as its exact form. Results are nearly identical. Pressure coefficients and velocity profiles (not shown) are also nearly identical.

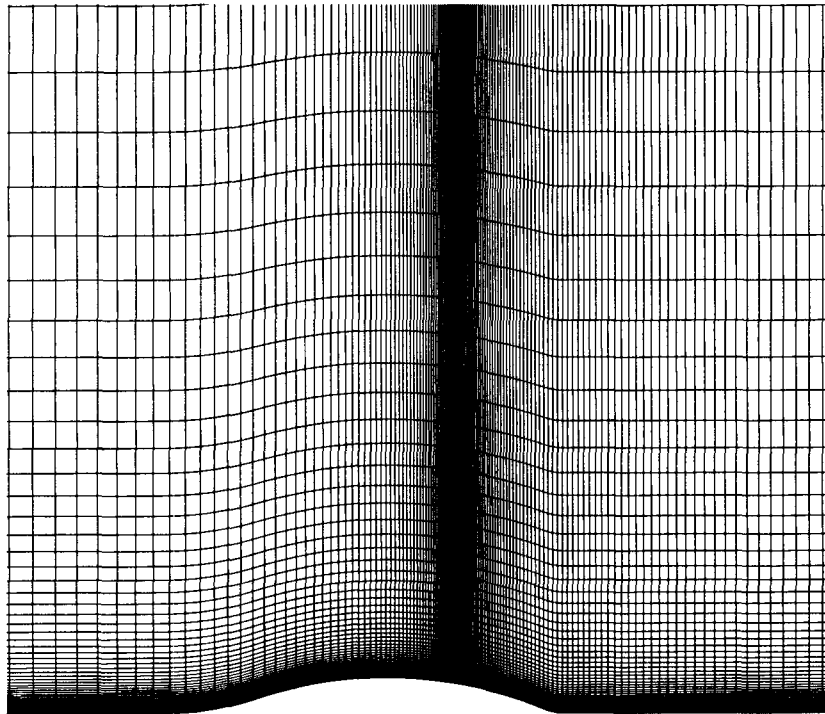


Figure 27: Axisymmetric bump grid, $181 \times 101 \times 2$.

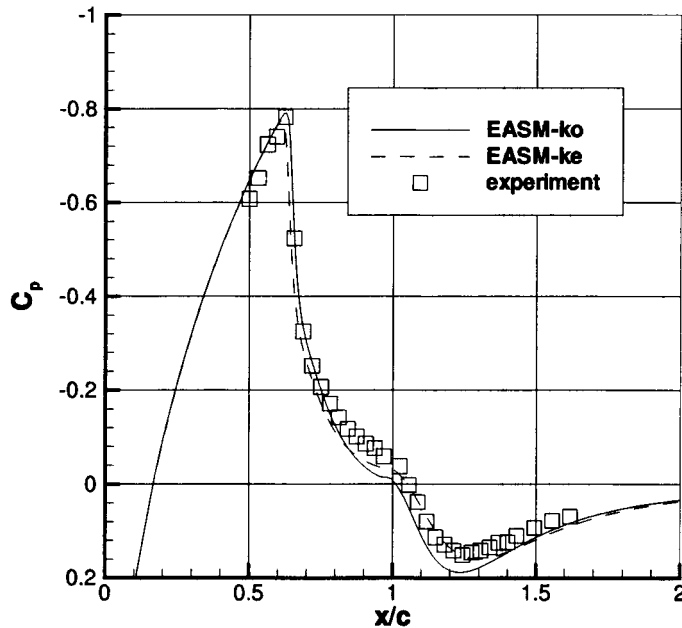


Figure 28: Surface pressure coefficients for axisymmetric bump.

4.7 ONERA M6 Wing

The ONERA M6 wing is a 3-D case often used to validate codes and turbulence models. The experimental data are from Schmitt and Charpin [33].

The particular case studied here has a Mach number of 0.84 and Reynolds number based on mean aerodynamic chord of 11.7×10^6 . The angle of attack is 3.06° . At these conditions, there are two shock waves across the inboard part of the wing upper surface, which merge to form a single shock wave at the outboard part of the wing. There is no significant flow separation for this case.

The grid used for this case is a C-O type grid of size $289 \times 65 \times 49$. Part of the grid (with every other grid point removed) is shown in Fig. 32. The grid is scaled so that the chord of the wing varies from 0.6737 at the root to 0.3789 at the tip. In these units, the Reynolds number per unit length is 21.66×10^6 . The grid extends to approximately -6.4 unit lengths upstream, 7.4 unit lengths downstream, 6.4 unit lengths high, and 7.4 unit lengths to the side. Symmetry conditions are applied along the center plane, and farfield conditions are applied at the farfield boundaries. There are 225 streamwise points and 49 spanwise points on the wing surface itself, for a total of 11025 surface points.

The average minimum normal spacing at the wall is approximately 6×10^{-6} unit lengths, which yields an average minimum y^+ value of the first cell center off the wall of approximately 3.2. This minimum spacing is larger than one would usually want to use for a turbulent flow computation. Based on the flat plate results in section 4.1, such a large wall spacing can yield skin friction levels that are more than 5% in error. However, it was still considered important

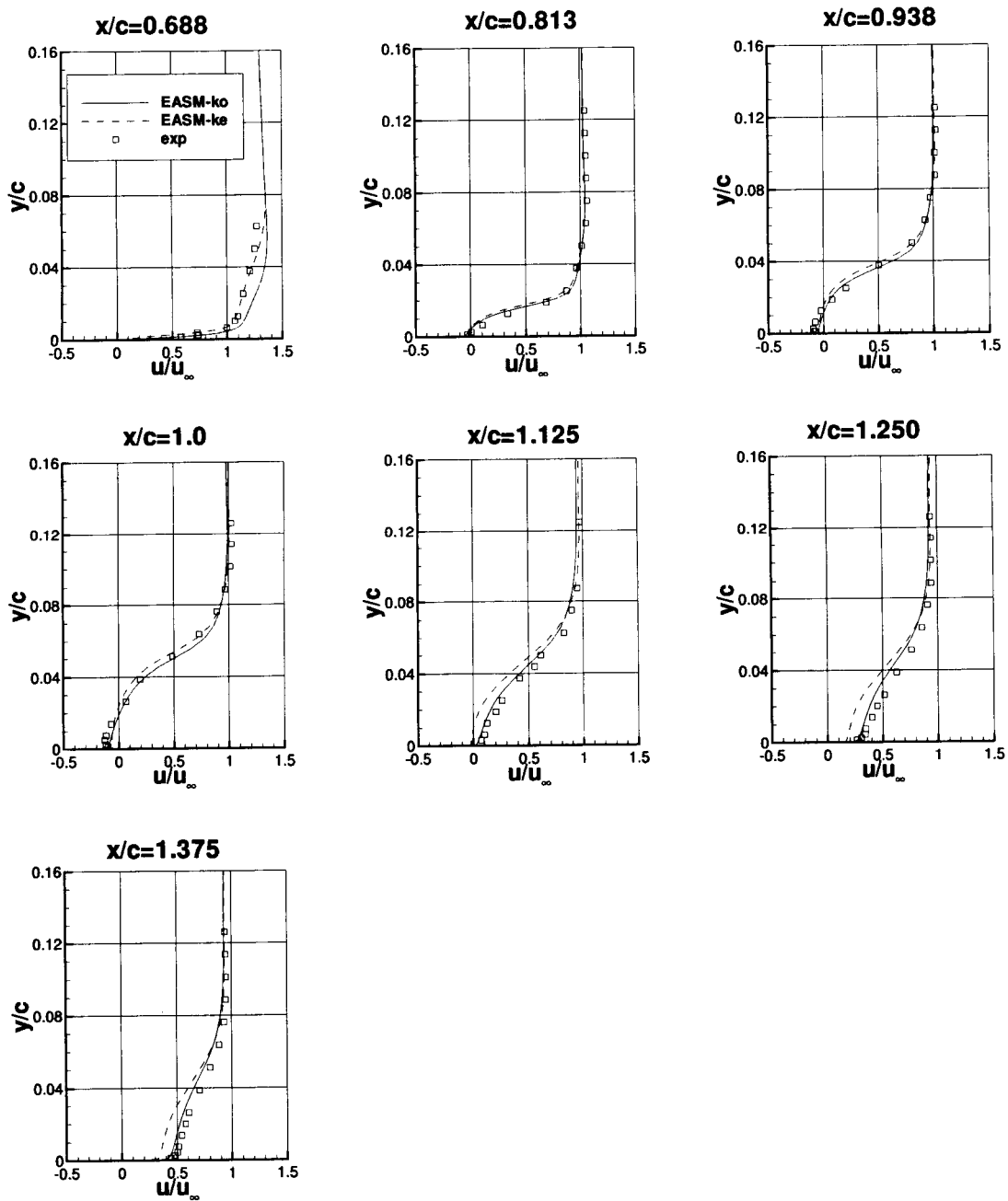


Figure 29: Velocity profiles for axisymmetric bump.

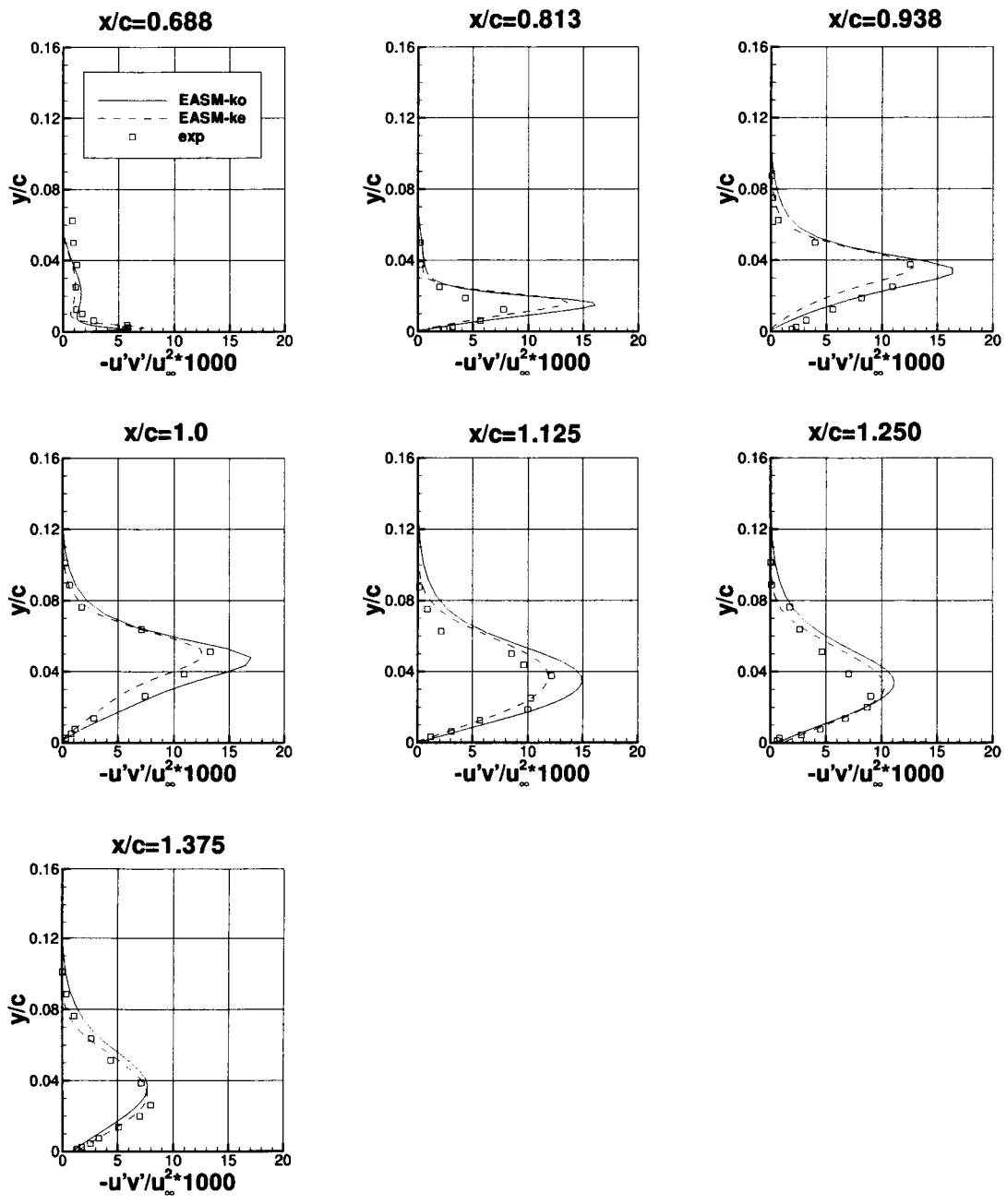


Figure 30: Turbulent shear stress profiles for axisymmetric bump.

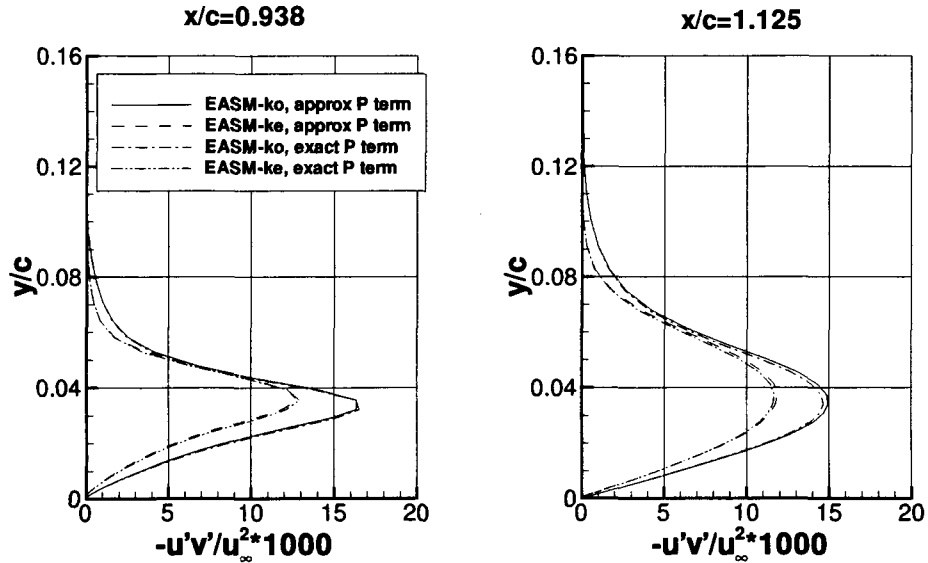


Figure 31: Effect of approximate production term on turbulent shear stress profiles for axisymmetric bump.

to include this case as a part of this validation archive because it demonstrates the capabilities of these models on a less-than-optimal grid (which is not an uncommon occurrence in many situations involving 3-D configurations).

Fig. 33 shows surface pressure coefficients at six span stations for the two models. Both do an excellent job capturing the pressure levels, including shock location.

4.8 2-D Airfoil Wake

This test case investigates the near-field development and decay of the 2-D wake of an airfoil at low Mach number. The experimental data are from Nakayama [34].

The case studied here uses the “Model A” airfoil, which is a 10% thick conventional airfoil. It is computed at a Mach number of 0.1 and Reynolds number based on chord of 1.2×10^6 (the chordlength is 24 inches). The angle of attack is 0° . At these conditions, there is no flow separation on the airfoil.

The grid used for this case is a C-grid, but it is divided into two zones. The first zone is 257×97 and consists of the part of the C-grid containing points on the airfoil surface (thus, there are 257 points on the airfoil surface). The second zone is 153×193 and consists of the part of the C-grid in the wake, with the top and bottom halves put together. The grid is shown in Fig. 34. The grid extent is approximately 20 chords, and the average minimum normal spacing at the wall is approximately 1×10^{-5} chords, which yields an average minimum y^+ value of the first cell center off the wall of approximately 0.5. In the wake, the minimum grid spacing occurs along the wake cut; it starts out with the same minimum spacing as at the airfoil, then spreads further downstream. For example, at $x/c = 1.2$, the minimum normal spacing on the centerline is approximately 1×10^{-4} chords. At that station there are approximately 97 grid

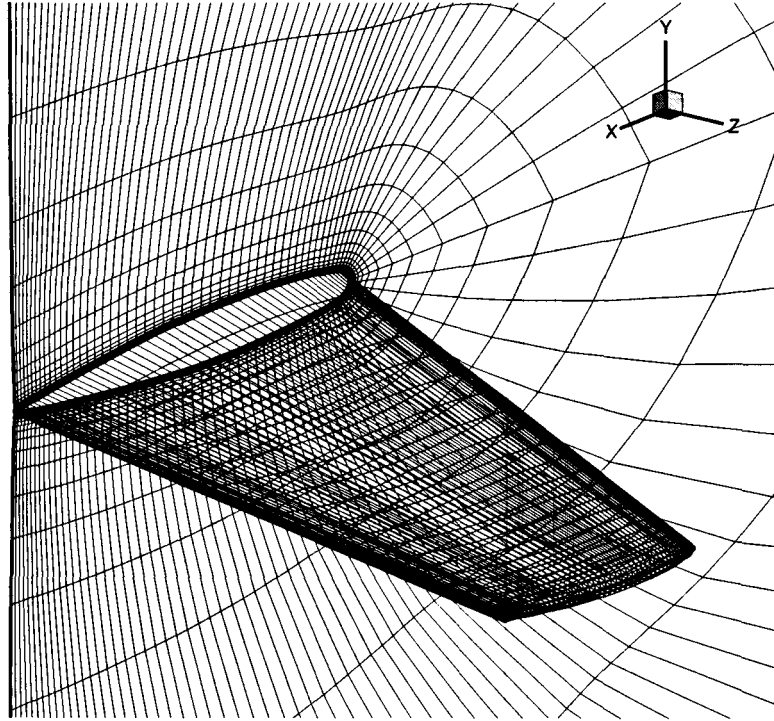


Figure 32: Schematic of ONERA M6 grid, $289 \times 65 \times 49$ (every other grid point shown).

points between $y = -1$ and 1 inches ($y/c = -0.0417$ and 0.0417).

Fig. 35 shows wake velocity profiles at seven streamwise stations for the two models. The EASM-ke has a slightly deeper maximum wake deficit than EASM-ko at stations downstream of $x/c = 1.2$, in better agreement with experiment, but EASM-ko yields a slightly better spreading rate in this case. Both models predict the wake position to be somewhat too low compared to experiment at the last two stations.

Fig. 36 shows wake turbulent shear stress profiles. Overall, both models agree well with experiment. The EASM-ke predicts higher peak levels than EASM-ko at the first two stations, then predicts slightly lower levels downstream. Both models underpredict the peak levels seen in the experiment at most of the stations downstream of $x/c = 1.2$.

4.9 Curved Duct in Zero Pressure Gradient

The curved duct test case was the subject of an extensive study in Rumsey et al.[35] related to curvature effects, and included the application of curvature corrections both to EASM-ke as well as to a linear one-equation model. However, the subject of the present paper is solely a validation for the “standard” forms of EASM-ko and EASM-ke, so curvature-corrected results are not presented here. (Nonetheless, it was found in Rumsey et al. that the “standard” form of EASM performs reasonably well for this case because EASM still retains some of the invariance properties of the full differential stress model. The more exact curvature-corrected version yielded only modest improvements.) The experimental data for this case are from So and Mellor [36].

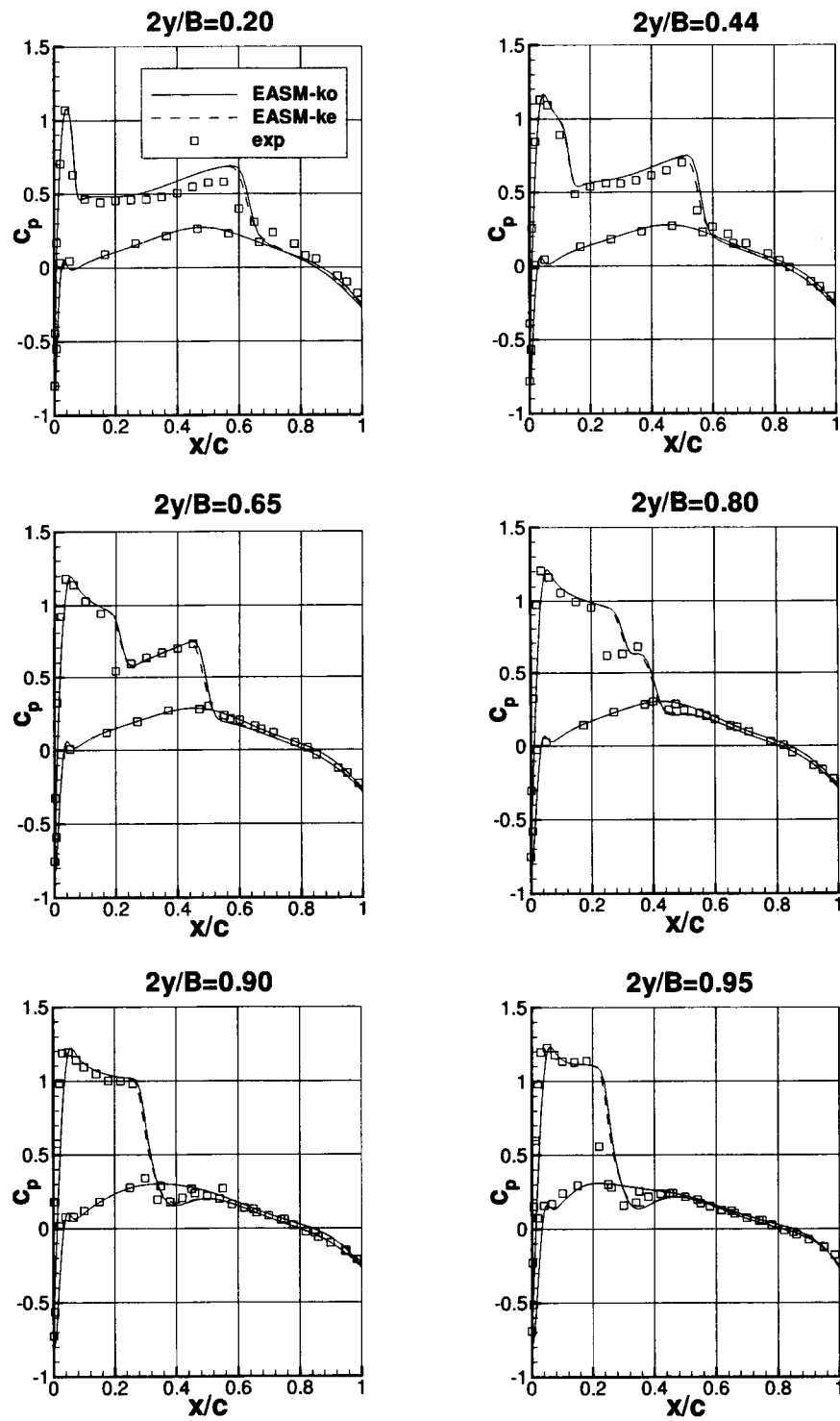


Figure 33: Surface pressure coefficients for ONERA M6.

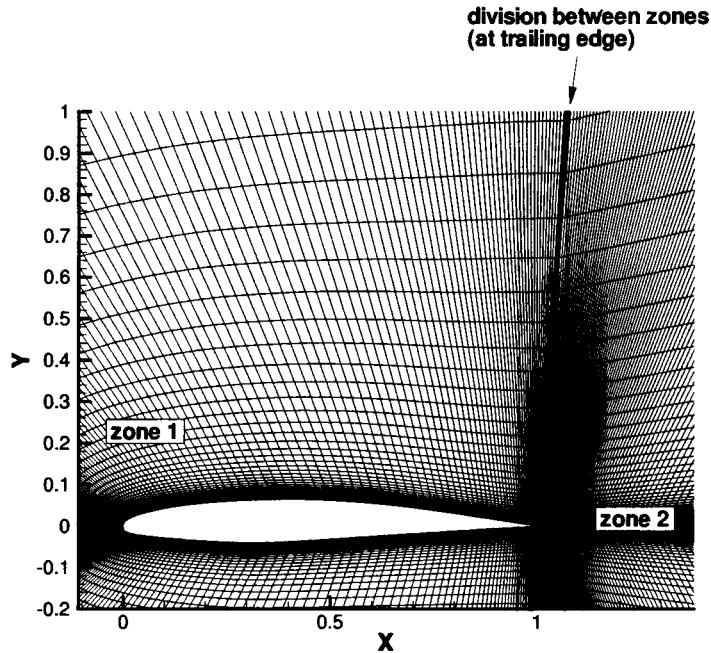


Figure 34: Nakayama model A grid, 257×97 and 153×193 .

This case is an internal flow with inner-wall convex curvature. The outer wall is shaped to yield approximately a zero streamwise pressure gradient along the inner wall in the region of interest. The Mach number at the inlet is 0.063, and the Reynolds number is taken to be 3.6417×10^4 per inch.

The grid used for this case is 129×81 , shown in Fig. 37. In this figure (and in those to follow), the coordinate s refers to distance measured along the inner wall, with $s = 24$ in. as the location of the inlet to the computational grid. A grid study was performed in Rumsey et al.[35], where it was concluded that this grid size is adequate. Slip-wall boundary conditions were applied at the outer wall in the CFD simulation. This boundary condition allowed the simulation to be run without the complication of having to contend with tangential air or bleed boundary conditions. The inner wall boundary condition was no-slip, adiabatic wall. The minimum normal spacing at the lower wall was 0.00015 in., which yields an average minimum y^+ value of the first cell center off the wall of less than 0.5. The outflow boundary condition set pressure at $p/p_{ref} = 1.0$ (where “ref” refers to inlet conditions), and extrapolated all other quantities. At the upstream boundary, the density, velocity, and turbulence quantities were set to closely match experiment (see Rumsey et al.[6] for details concerning this procedure). The pressure at the inflow was extrapolated from the interior of the domain.

Fig. 38 shows surface skin friction coefficient along the inner wall. Both EASM-ko and EASM-ke give reasonable agreement with experiment. Velocity profiles (referenced to inlet conditions and local boundary layer thickness) are shown in Fig. 39. These are predicted in good agreement with experiment. Turbulence quantities are given in Figs. 40, 41, and 42. Note that all turbulent shear and normal stresses are in the local body/normal coordinate system.

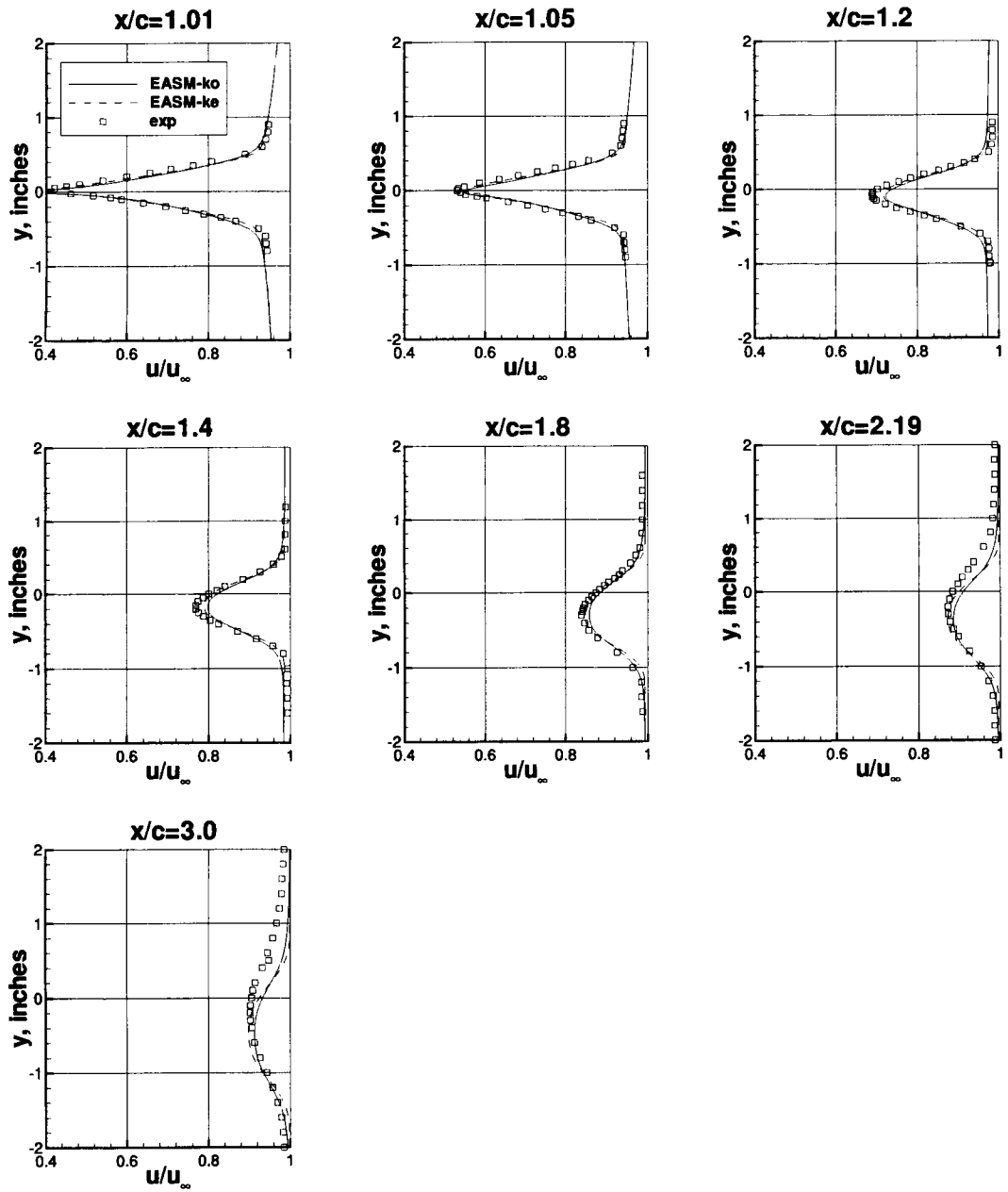


Figure 35: Wake velocity profiles for Nakayama model A.

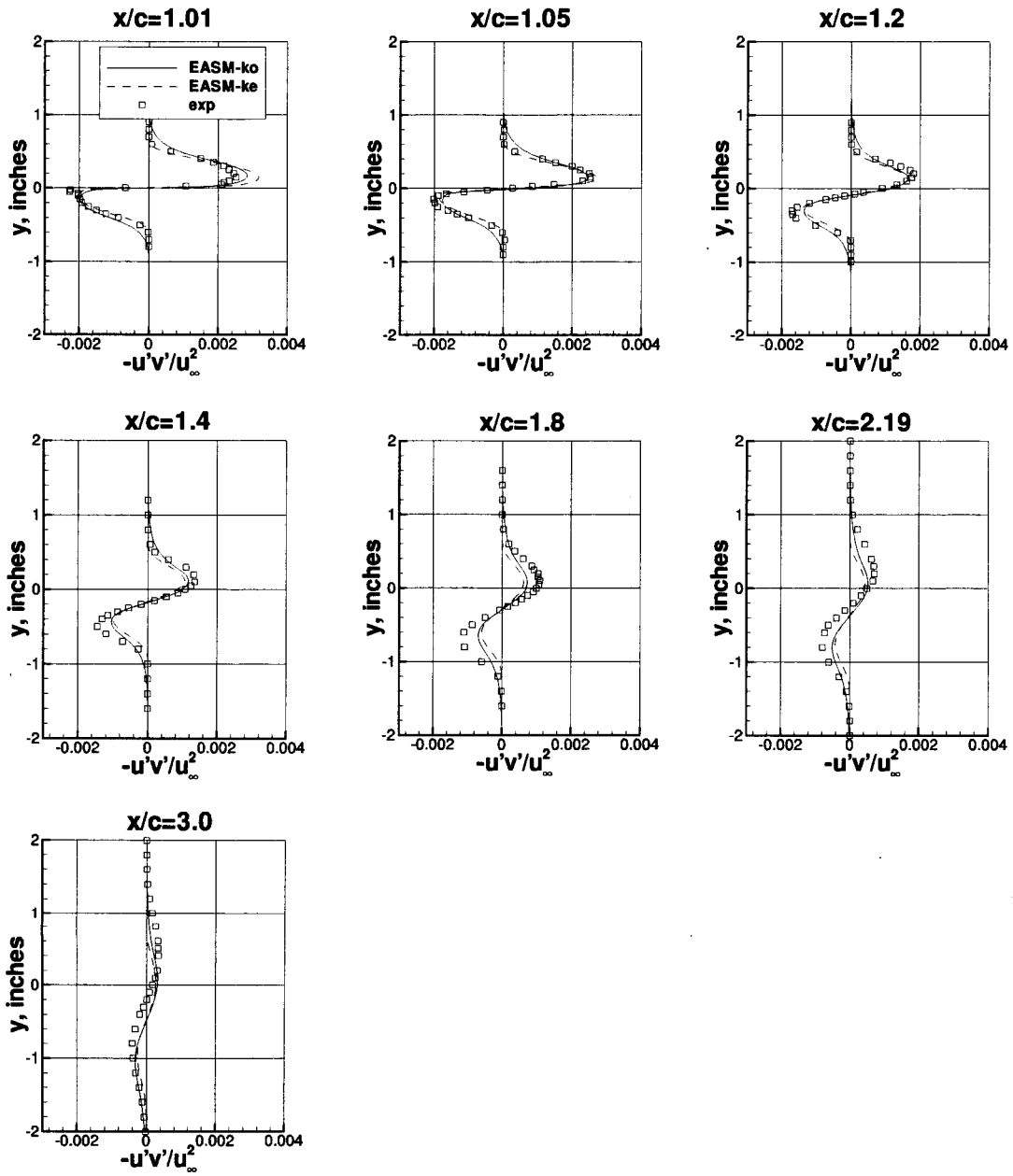


Figure 36: Wake turbulent shear stress profiles for Nakayama model A.

Stresses in this frame are related to those in the Cartesian frame by the following relations:

$$\overline{u'v'} = \frac{1}{2}(\overline{v'v'}_c - \overline{u'u'}_c)\sin(2\Theta) + \overline{u'v'}_c\cos(2\Theta) \quad (42)$$

$$\overline{u'u'} = \overline{u'u'}_c\cos^2\Theta + \overline{v'v'}_c\sin^2\Theta + \overline{u'v'}_c\sin(2\Theta) \quad (43)$$

$$\overline{v'v'} = \overline{v'v'}_c\cos^2\Theta + \overline{u'u'}_c\sin^2\Theta - \overline{u'v'}_c\sin(2\Theta), \quad (44)$$

where the subscript c indicates Cartesian frame, and Θ is the angle that the body tangent vector makes with the x -axis.

The $u'u'$ turbulent normal stress levels are predicted somewhat too large in magnitude by the EASM models in the curved region of the duct, but the turbulent shear stresses and the $v'v'$ normal stresses are predicted in good agreement with experiment.

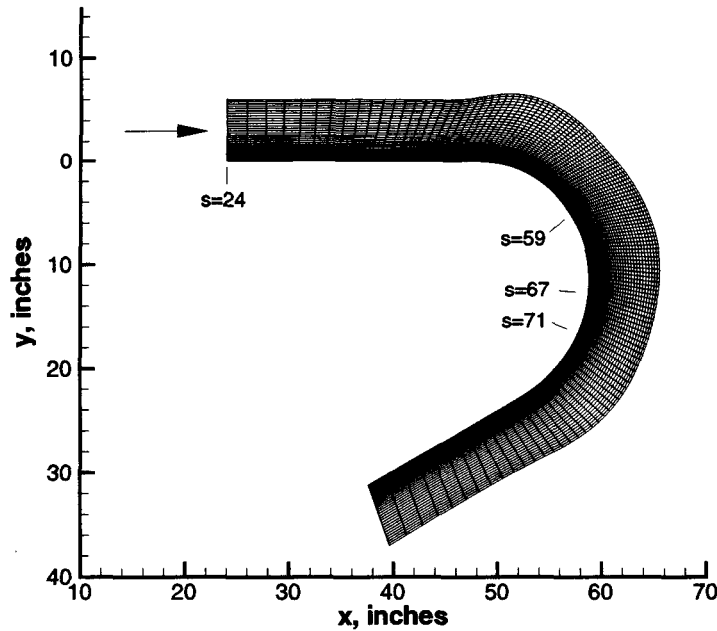


Figure 37: Curved duct grid, 129×81 .

5 CONCLUSIONS

In conclusion, this paper summarized the Explicit Algebraic Stress Model in $K-\omega$ form (EASM-ko) and in $K-\varepsilon$ form (EASM-ke) in the Reynolds-averaged Navier-Stokes code CFL3D. Details of the equations and method for coding the latest versions of the models were given, and numerous validation cases were presented. Except for the well-known problem of the standard form of the ε equation being ill-suited for wall-bounded adverse pressure gradient flows, both of these models were shown to yield good results for a wide variety of different cases. These cases included flow fields with shock waves, curvature, and significant regions of separation.

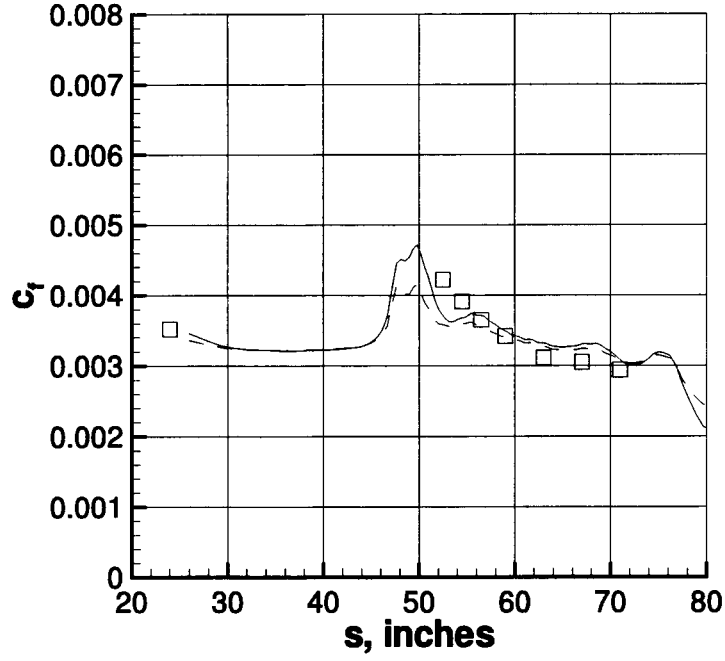


Figure 38: Surface skin friction coefficient, referenced to inlet conditions.

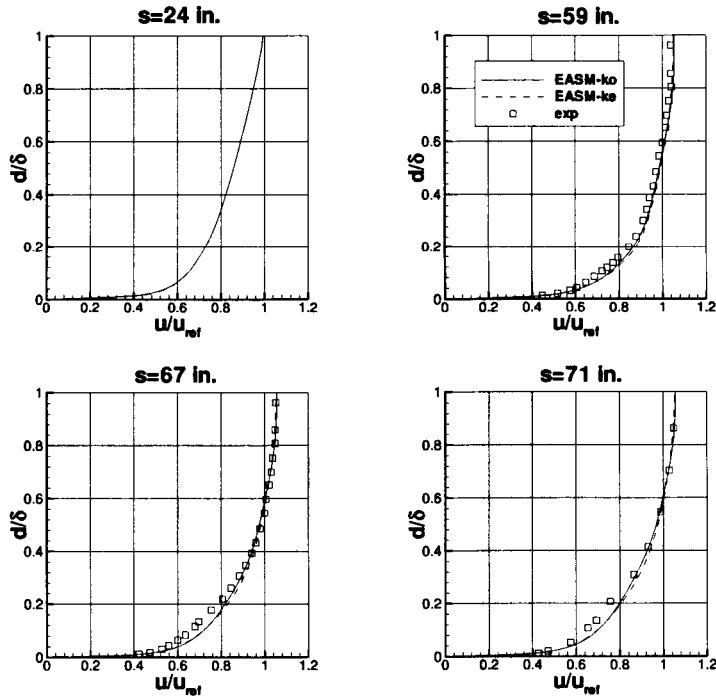


Figure 39: Velocity profiles, referenced to inlet conditions.

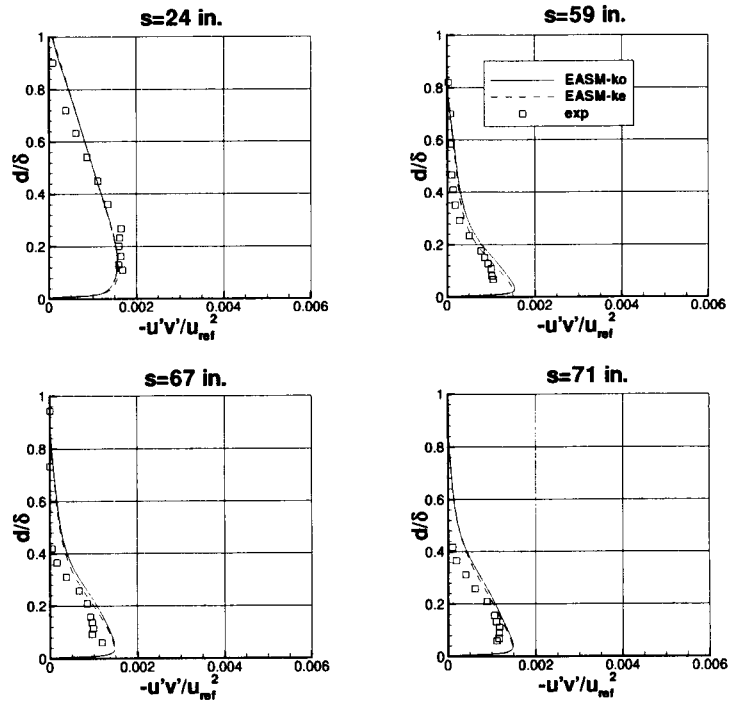


Figure 40: Turbulent shear stress profiles, referenced to inlet conditions.

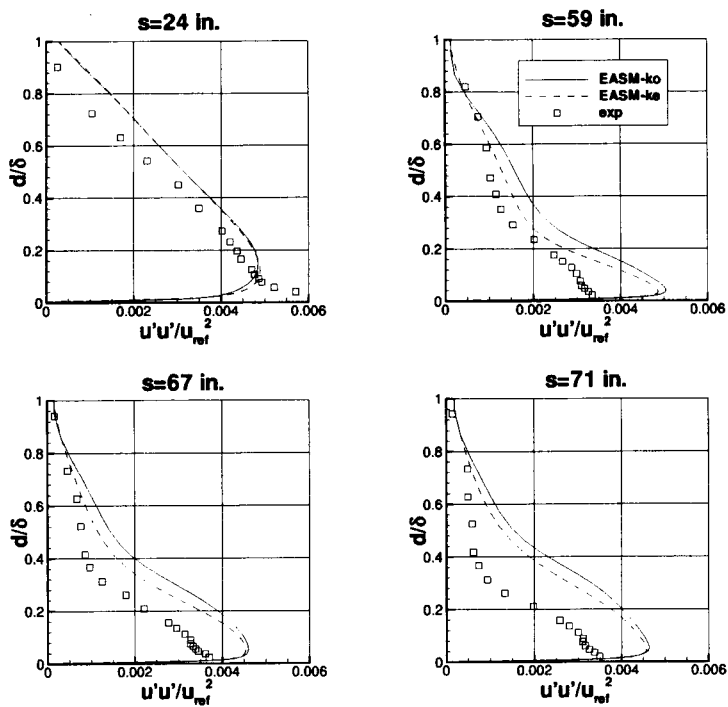


Figure 41: Turbulent $u'u'$ normal stress profiles, referenced to inlet conditions.

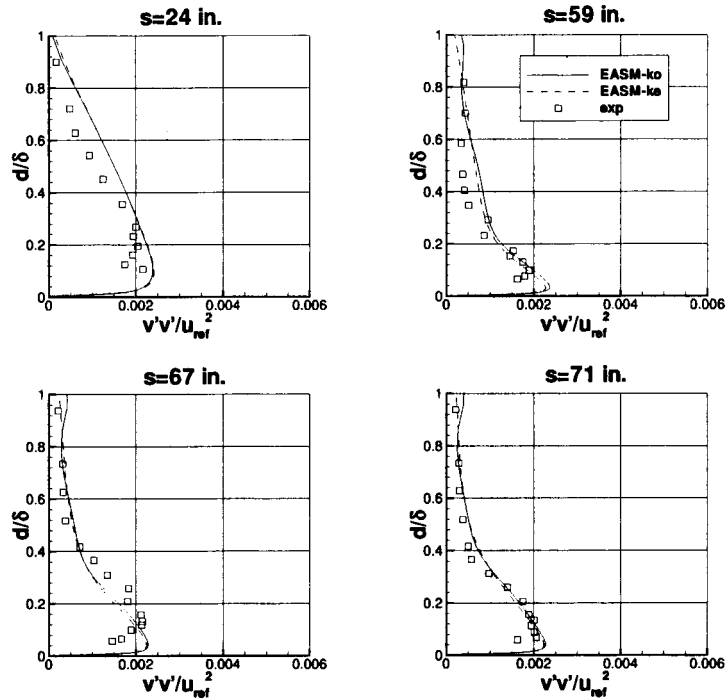


Figure 42: Turbulent $v'v'$ normal stress profiles, referenced to inlet conditions.

References

- [1] Abdol-Hamid, K. S., Lakshmanan, B., and Carlson, J. R., "Application of Navier-Stokes Code PAB3D with $k-\epsilon$ Turbulence Model to Attached and Separated Flows," NASA TP-2480, January 1995.
- [2] Gatski, T. B. and Rumsey, C. L., "Linear and Nonlinear Eddy Viscosity Models," in *Closure Strategies for Turbulent and Transitional Flows*, ed. B. E. Launder and N. D. Sandham, Cambridge University Press, Cambridge U. K., 2002.
- [3] Gatski, T. B. and Speziale, C. G., "On Explicit Algebraic Stress Models for Complex Turbulent Flows," *Journal of Fluid Mechanics*, Vol. 254, 1993, pp. 59–78.
- [4] Ying, R., and Canuto, V. M., "Turbulence Modelling over Two-Dimensional Hills Using an Algebraic Reynolds Stress Expression," *Boundary-Layer Meteorology*, Vol. 77, 1996, pp. 69–99.
- [5] Girimaji, S. S., "Fully Explicit and Self-Consistent Algebraic Reynolds Stress Model," *Theoret. Comput. Fluid Dynamics*, Vol. 8, 1996, pp. 387–402.
- [6] Rumsey, C. L., Gatski, T. B., and Morrison, J. H., "Turbulence Model Predictions of Strongly Curved Flow in a U-Duct," *AIAA Journal*, Vol. 38, No. 8, 2000, pp. 1394–1402.
- [7] Carlson, J. R., "Applications of Algebraic Reynolds Stress Turbulence Models, Parts 1 and 2," *Journal of Propulsion and Power*, Vol. 13, No. 5, 1997, pp. 610–628.

- [8] Carlson, J. R., Duquesne, N., Rumsey, C. L., and Gatski, T. B., "Computation of Turbulent Wake Flows in Variable Pressure Gradient," *Computers & Fluids*, Vol. 30, 2001, pp. 161-187.
- [9] Krist, S. L., Biedron, R. T., and Rumsey, C. L., "CFL3D User's Manual (Version 5.0)," NASA TM-1998-208444, June 1998.
- [10] Weiss, J. M., and Smith, W. A., "Preconditioning Applied to Variable and Constant Density Flows," *AIAA Journal*, Vol. 33, No. 11, 1995, pp. 2050-2057.
- [11] Roe, P. L., "Approximate Riemann Solvers, Parameter Vectors, and Difference Schemes," *J. Computational Physics*, Vol. 43, 1981, pp. 357-372.
- [12] Wilcox, D. W., *Turbulence Modeling For CFD*, 2nd ed., DCW Industries, La Canada, 1998.
- [13] Favre, A., "Equations des Gaz Turbulents Compressibles," *J. Mecanique*, Vol. 4, No. 3, 1965, pp. 361-390.
- [14] Jongen, T. and Gatski, T. B., "General Explicit Algebraic Stress Relations and Best Approximation for Three-Dimensional Flows," *Int. J. of Engineering Science*, Vol. 36, 1998, pp. 739-763.
- [15] Rumsey, C. L., and Gatski, T. B., "Recent Turbulence Model Advances Applied to Multi-element Airfoil Computations," *J. Aircraft*, Vol. 38, No. 5, 2001, pp. 904-910.
- [16] Jongen, T., and Gatski, T. B., "A Unified Analysis of Planar Homogeneous Turbulence Using Single-Point Closure Equations," *Journal of Fluid Mechanics*, Vol. 399, 1999, pp. 117-150.
- [17] Georgiadis, N. J., Rumsey, C. L., Yoder, D. A., and Zaman, K. B. M. Q., "Effects of RANS Turbulence Modeling on Calculation of Lobed Nozzle Flowfields," AIAA Paper 2003-1271, January 2003.
- [18] Warsi, Z. U. A., *Fluid Dynamics, Theoretical and Computational Approaches*, CRC Press, Inc., Boca Raton, 1993, pp. 544-454.
- [19] Menter, F. R., "Two-Equation Eddy-Viscosity Turbulence Models for Engineering Applications," *AIAA Journal*, Vol. 32, No. 8, 1994, pp. 1598-1605.
- [20] Biedron, R. T., CFL3D V6 webpage, <<http://cfl3d.larc.nasa.gov/Cfl3dv6/cfl3dv6.html>>, 2003.
- [21] White, F. M., *Viscous Fluid Flow*, McGraw-Hill Book Company, New York, 1974.
- [22] Driver, D. M. and Seegmiller, H. L., "Features of a Reattaching Turbulent Shear Layer in Divergent Channel Flow," *AIAA Journal*, Vol. 23, No. 2, 1985, pp. 163-171.
- [23] Johnson, D. A., Menter, F. R., and Rumsey, C. L., "The Status of Turbulence Modeling for External Aerodynamics," AIAA Paper 94-2226, June 1994.
- [24] Sajben, M., and Kroutil, J.C., "Effects of Initial Boundary-Layer Thickness on Transonic Diffuser Flows," *AIAA Journal*, Vol. 19, No. 11, 1981, pp. 1386-1393.
- [25] Slater, J. W., NPARC Alliance Validation Archive, <<http://www.grc.nasa.gov/www/wind/valid/transdif/transdif02/transdif02.html>>, 2003.

- [26] Coles, D. and Wadcock, A. J., "Flying-Hot-Wire Study of Flow Past an NACA 4412 Airfoil at Maximum Lift," *AIAA Journal*, Vol. 17, No. 4, 1979, pp. 321–329.
- [27] Rodi, W., and Scheuerer, G., "Scrutinizing the $K-\varepsilon$ Turbulence Model Under Adverse Pressure Gradient Conditions," *Journal of Fluids Engineering*, Vol. 108, No. 6, 1986, pp. 174–179.
- [28] Nagano, Y., and Tagawa, M., "An Improved $K-\varepsilon$ Model for Boundary Layer Flows," *Journal of Fluids Engineering*, Vol. 112, No. 3, 1990, pp. 33–39.
- [29] Gilbert, G. B. and Hill, P. G., "Analysis and Testing of Two-Dimensional Slot Nozzle Ejectors with Variable Area Mixing Sections," NASA CR-2251, May 1973.
- [30] Georgiadis, N. J., Yoder, D. A., and DeBonis, J. R., "A Comparison of Three Navier-Stokes Solvers for Exhaust Nozzle Flowfields," AIAA Paper 99-0748, January 1999.
- [31] Bachalo, W. D. and Johnson, D. A., "An Investigation of Transonic Turbulent Boundary Layer Separation Generated on an Axisymmetric Flow Model," AIAA Paper 79-1479, June 1979.
- [32] Menter, F. R. and Rumsey, C. L., "Assessment of Two-Equation Turbulence Models for Transonic Flows," AIAA Paper 94-2343, June 1994.
- [33] Schmitt, V. and Charpin, F., "Pressure Distributions on the ONERA M6 Wing at Transonic Mach Numbers," AGARD AR-138, May 1979, p. B1.
- [34] Nakayama, A., "Characteristics of the Flow Around Conventional and Supercritical Airfoils," *J. Fluid Mech.*, Vol. 160, 1985, pp. 155–179.
- [35] Rumsey, C. L., Gatski, T. B., Anderson, W. K., and Nielsen, E. J., "Isolating Curvature Effects in Computing Wall-Bounded Turbulent Flows," *Int. J. Heat and Fluid Flow*, Vol. 22, 2001, pp. 573–582.
- [36] So, R. M. C. and Mellor, G. L., "Experiment on Convex Curvature Effects in Turbulent Boundary Layers," *J. Fluid Mech.*, Vol. 60, Part 1, 1973, pp. 43–62.

REPORT DOCUMENTATION PAGE			Form Approved OMB No. 0704-0188	
Public reporting burden for this collection of information is estimated to average 1 hour per response, including the time for reviewing instructions, searching existing data sources, gathering and maintaining the data needed, and completing and reviewing the collection of information. Send comments regarding this burden estimate or any other aspect of this collection of information, including suggestions for reducing this burden, to Washington Headquarters Services, Directorate for Information Operations and Reports, 1215 Jefferson Davis Highway, Suite 1204, Arlington, VA 22202-4302, and to the Office of Management and Budget, Paperwork Reduction Project (0704-0188), Washington, DC 20503.				
1. AGENCY USE ONLY (Leave blank)		2. REPORT DATE June 2003	3. REPORT TYPE AND DATES COVERED Technical Memorandum	
4. TITLE AND SUBTITLE Summary of EASM Turbulence Models in CFL3D With Validation Test Cases			5. FUNDING NUMBERS 762-20-11-06	
6. AUTHOR(S) Christopher L. Rumsey and Thomas B. Gatski				
7. PERFORMING ORGANIZATION NAME(S) AND ADDRESS(ES) NASA Langley Research Center Hampton, VA 23681-2199			8. PERFORMING ORGANIZATION REPORT NUMBER L-18311	
9. SPONSORING/MONITORING AGENCY NAME(S) AND ADDRESS(ES) National Aeronautics and Space Administration Washington, DC 20546-0001			10. SPONSORING/MONITORING AGENCY REPORT NUMBER NASA/TM-2003-212431	
11. SUPPLEMENTARY NOTES				
12a. DISTRIBUTION/AVAILABILITY STATEMENT Unclassified-Unlimited Subject Category 02 Distribution: Nonstandard Availability: NASA CASI (301) 621-0390			12b. DISTRIBUTION CODE	
13. ABSTRACT (Maximum 200 words) This paper summarizes the Explicit Algebraic Stress Model in k-omega form (EASM-ko) and in k-epsilon form (EASM-ke) in the Reynolds-averaged Navier-Stokes code CFL3D. These models have been actively used over the last several years in CFL3D, and have undergone some minor modifications during that time. Details of the equations and method for coding the latest versions of the models are given, and numerous validation cases are presented. This paper serves as a validation archive for these models.				
14. SUBJECT TERMS Turbulence model; Validation; Explicit algebraic stress; Separated flow			15. NUMBER OF PAGES 48	
			16. PRICE CODE	
17. SECURITY CLASSIFICATION OF REPORT Unclassified	18. SECURITY CLASSIFICATION OF THIS PAGE Unclassified	19. SECURITY CLASSIFICATION OF ABSTRACT Unclassified	20. LIMITATION OF ABSTRACT UL	